SURFACE PLASMON COUPLED SENSOR AND NANOLENS

A Dissertation

by

HYUNGDUK KO

Submitted to the Office of Graduate Studies of
Texas A&M University
in partial fulfillment of the requirements for the degree of

DOCTOR OF PHILOSOPHY

May 2009

Major Subject: Electrical Engineering

SURFACE PLASMON COUPLED SENSOR AND NANOLENS

A Dissertation

by

HYUNGDUK KO

Submitted to the Office of Graduate Studies of
Texas A&M University
in partial fulfillment of the requirements for the degree of

DOCTOR OF PHILOSOPHY

Approved by:

Co-Chairs of Committee,	Chin B. Su
	Mosong Cheng
Committee Members,	Arum Han
	Yue Kuo
Head of Department,	Costas N. Georghiades

May 2009

Major Subject: Electrical Engineering

ABSTRACT

Surface Plasmon Coupled Sensor and Nanolens.

(May 2009)

Hyungduk Ko, B.S. ; M.S., Korea University

Co-Chairs of Advisory Committee: Dr. Chin B. Su
Dr. Mosong Cheng

This dissertation consists of two topics. One is a "Multi-pass Fiber Optic Surface Plasmon Resonance Sensor (SPR)" and the other is a "Nano-metallic Surface Plasmon Lens." Since both topics involved surface plasmon, the title of this dissertation is named "Surface plasmon coupled sensor and nanolens."

For a multi-pass fiber optic SPR sensor, a fiber optic 4-pass SPR sensor coupled with a field-assist capability for detecting an extremely low concentration of charged particles is first demonstrated. The multipass feature increases the sensitivity by a factor equal to the number of passes. The field-assist feature forces charged particles/molecules to the SPR surface, increasing the sensitivity by an additional factor of about 100. Overall, the sensitivity exceeds the one-pass SPR device by a factor of about 400. A 10 pM concentration of 47 nm diameter polystyrene (PS) latex beads and 1 μM concentration of salt dissolved in DI water were detected within a few seconds by the combined system. The equivalent index resolution for atomic size corresponding to ionized chlorine in salt is 10^{-8}. This technique offers the potential for sensitive and fast detection of biomolecules in a solution. Secondly, a 44-pass fiber optic surface plasmon resonance (SPR) sensor coupled with a field-assist capability for measurement of

refractive index change due to positive and negative ions is shown. The field-assist feature forces ions to the SPR surface, causing the SPR signal response to change which reflects a decrease or increase in refractive index depending on whether positive or negative ions are being attracted to the surface. This technique offers the potential for the sensitive detection of cations and anions in a solution.

For a nano-metallic surface plasmon lens, we analyze the transmission of a normally incident plane wave through an Ag/dielectric layered concentric ring structure using finite difference time domain (FDTD) analysis. The dependency of the transmission efficiency on the refractive index in slit is studied. The numerical analysis indicates that the focusing beyond diffraction limit is found even at the extended focal length comparable to the distance of 7λ from the exit plane using a circularly polarized coherent plane wave, λ=405 nm. Especially, compared to an Ag-only structure, the Ag/ $LiNbO_3$ structure amplifies the transmission power by a factor of 6. Therefore, this Ag/dielectric layered lens has the potential for significantly higher resolution imaging and optical data storage.

DEDICATION

To my parents

ACKNOWLEDGEMENTS

It has been a long journey to earn my Ph. D. degree. First of all, I would like to express my sincere appreciation to the chairs of my committee, Dr. Chin B. Su and Dr. Mosong Cheng. Without their advices and support, this study could not have been achievable. During the last 5 years, I have been impressed and have learned many things in science, as well as life, by which I hope to make my future model and portrait. I am also deeply grateful to Dr. Arum Han and Dr. Yue Kuo, members of the advisory committee who gave me great advice on this dissertation.

I am very thankful to the Solid State Electronics Group colleagues, Hyunchul Kim, Yongwook Shin, Sungkyu Seo, Hyunsoo Park, Jungmoo Hong, Jaewon Park, Jaewoo Seo and Hyunsoo Kim for their invaluable assistance and wonderful friendship during my Ph.D. courses. I am also thankful to Tammy for her technical assistance. In addition, I truly appreciate all my Korean Catholic Community friends at St. Mary's who prayed for and encouraged me.

Finally, I would like to share my pleasure in completing this study with my family who have waited such a long time for this moment.

TABLE OF CONTENTS

Page

Page

LIST OF FIGURES

Page

Page

Page

Page

CHAPTER I

INTRODUCTION

1.1 Organization of the Dissertation

This dissertation consists of two topics. One is a "Multi-pass Fiber Optic Surface Plasmon Resonance Sensor" and the other is a "Nano-metallic Surface Plasmon Lens." Since both topics involved surface plasmon, the title of this dissertation is named "Surface plasmon coupled sensor and nanolens."

Chapter I discusses the objective of the proposed research topics as an introduction to the dissertation.

Chapter II consists of a brief theoretical review. The theory section consists of wave equation, surface plasmon solution, conventional SPR sensor, finite-difference-time-domain (FDTD) simulation, diffraction limit and wave propagation mode in subwavlength slit.

Chapter III discusses experiment apparatus, experiment results, and gives a brief summary of field-assist four-pass SPR sensor.

Chapter IV provides experiment apparatus, experiment results, and gives a brief summary of forty four-pass SPR sensor.

Chapter V discusses the numerical study on metallic/dielectric nano-optic lens.

This dissertation follows the style of Journal of Vacuum Science and Technology B.

1.2 Multi-pass Surface Plasmon Resonance Sensor

Recently, great progress in nanotechnology has made possible the detection of very low concentration of molecules using electrical, optical and mechanical techniques such as the nanowire field effect transistor (FET),[1] photon-tunneling sensor,[2] and nanocantilevers.[3] Surface plasmon resonance (SPR) sensor has attracted much attention for chemical and biological sensing in the last two decades because it allows real-time detection of biological species without the need of labeled molecules [4-18]. It detects physical phenomena occurring at surfaces, allowing the study of molecule affinities such as antibody-antigen, ligand-receptor, and protein-nucleic acid interactions[4,5]. Fundamentally, surface plasmons (SPs) are charge density waves that propagate along the surface of metals when an optical wave at an incident excitation angle impinges the metal- dielectric interface.[8] Generally, SPR is implemented using the Kretschmann's configuration[9] with a light source and a detector on opposite sides of a prism, which allows for one reflection (one pass) of the optical beam off a very thin gold layer. When the incident light beam is at a certain resonance angle, the reflectivity exhibits a minimum value. The magnitude of the evanescent optical field associated with surface plasmon has a maximum value at the metal-dielectric interface and decay exponentially away from the dielectric media.[8, 10] A SPR sensor utilizes this evanescent optical wave localized just above a very thin metal surface to detect molecules. Perturbations of the evanescent field by molecules change the angle at resonant and were often used as a mean for the detection of molecules.[2]

Recently, Su et al. reported the 4-pass SPR sensor that enhanced the sensitivity by a factor equal to the number of pass through the sample.[19, 20] This multi-pass system allows for a higher sensitivity than the one-pass Kretschmann's SPR sensor.[9]

Firstly, in this dissertation, the 4-pass feature is incorporated with a field assist (applied voltage) method to our SPR sensor to measure charged particles in a solution to demonstrate its sensitivity. Overall, the sensitivity is enhanced by a factor of about 100 with an applied voltage, depending on particle's size under measurement. In this field-assist method, an electric field is applied across an analyte solution placed on a gold surface that functions as one of the two electrodes. The electric field causes the charged particles or ions to collect at the Au surface, effectively increasing the concentration of particles at the SPR surface to be sensed by the evanescent field. Secondly, SPR sensor with 44 pass fiber-optic loop is demonstrated. This system has the capability to detect both charged and uncharged analytes with the sensitivity enhancement by a factor of 44. In this dissertation, the 44 pass feature incorporated with the field-assist method is studied. We found for the first time that positive ions contribute to a decrease in refractive index while negative ions contribute to an increase in refractive index compare with the equilibrium solution. Because ions such as Na^+, K^+, H^+ are important in biological processes, the detection of these ions by SPR may be a new technique for the studies of such processes.

1.3 Light Transmission Through a Metal/Dielectric Nano Optic Lens

The diffraction limit is a big problem for the application of microscopy, lithography, data storage, etc. The manipulation of light using surface plasmon (SP) excitation or evanescent wave in metallic nanostructure have made possible extraordinary enhancement of transmission and beam shaping.[21-39] Especially, the study on super-resolution focusing or imaging beyond diffraction limit have attracted great attention for the application of nanolithography, [40-42] bio imaging [1,2,43] and optical data storage. [44-47] However, many studies on obtaining super resolution light spot have been achieved in near-field region and it is still big challenge to realize light spot with super resolution in far-field. For example, Liu *et al.*[26] reported a plasmonic lens to excite SPs toward the focal points. They demonstrated that the plasmonic lens enables the energy to be guided toward the focal point of the lens because a fraction of the incident light is coupled to the SPP. However, the guided light toward the focal point still had the limited propagation length within a fraction of the illumination wavelength along the direction to exit plane.

In order to realize light spot with super resolution in the extended focal length, Seo *et al*.[48] proposed a novel photonic device that functions as a nano scale objective lens. It consists of periodic sub-wavelength concentric ring features in a metal film coated on a quartz substrate. The device focuses the incident light to create a narrow beam in the near field and quasi-far field region. The focal beam propagates up to several wavelengths before it diverges. Moreover, the focal beam had much larger working distance (probe to sample distance is 1.7 μm or more) and enabled 95 nm

resolution maskless lithography (95 nm spots and lines) with 405 nm light source. This focusing quality is beyond the diffraction limit in optics. This improved focusing quality would also allow for high speed scanning, large field-of-view and significantly improved image contrast, and imaging details. However, in spite of the improve focusing quality of the device, the transmission power of the device is still not very good at the focal point and also the resolution is required to be improved.

In this dissertation, a Ag/dielectric nano-optic lens is proposed, which creates the focal spot with sub-wavelength resolution and high transmission power at the extended focal length. Using finite-difference and time-domain (FDTD) method, we analyzed the light transmission of a normally incident plane wave through a Ag/dielectric layered concentric ring structure and we found that a spatial resolution is beyond the diffraction limit at the focal length of 'mid-field' comparable to 7λ. In order to create the focal spot beyond diffraction limit, a large band of the enhanced evanescent waves or SP waves should be converted into the propagating waves in free space. [18] This proposed lens allows the enhanced evanescent waves or SP waves to be propagated up to the distance of the quasi far-field, therefore, it makes possible the improved resolution at the extended focal length.

CHAPTER II

THEORETICAL BACKGROUND

This chapter presents the theoretical backgrounds associated with surface plasmon resonance sensing and plasmonic lens. The fundamental equations of electromagnetic phenomenon, surface plasmon solution, SPR sensor techniques, Drude model and wave propagation in subwavelength structure are explained.

2.1 Surface Plasmon Resonance Sensor

2.1.1 Electromagnetic Waves and Matter

Maxwell's equations are the fundamental equations of electromagnetic phenomenon in a homogeneous, lossless, isotropic and source-free dielectric medium. They are expressed as bellows (references 49 and 50 are summarized and referred for the derivation, respectively):

$$\nabla \times \mathbf{E} = -\frac{\partial \mathbf{B}}{\partial t} \tag{2.1a}$$

$$\nabla \times \mathbf{H} = \frac{\partial \mathbf{D}}{\partial \mathbf{t}} + \mathbf{J} \tag{2.1b}$$

$$\nabla \cdot \mathbf{D} = 0 \tag{2.1c}$$

$$\nabla \cdot \mathbf{B} = 0 \tag{2.1d}$$

where **E** and **H** represent electric and magnetic field intensity vectors, **D** is the electric displacement vector, and **B** is the magnetic displacement vector. If we assume that the

materials are linearly polarized and magnetized in terms of the external fields, **D** and **B** can be defined as follows:

$$\mathbf{D} = \varepsilon_0 \mathbf{E} + \mathbf{P} = \varepsilon \mathbf{E} \tag{2.2a}$$

$$\mathbf{B} = \mu_0 \mathbf{H} \tag{2.2b}$$

Where **P** is the dielectric polarization density ($\mathbf{P}=\varepsilon_0(\varepsilon_r-1)\mathbf{E}$), ε_0 is the dielectric permittivity of free space, ε_r is the relative permittivity and μ_0 the magnetic permeability of free space. From the vector identity $\mathbf{A}\times\mathbf{B}\times\mathbf{C} = \mathbf{B}(\mathbf{A}\cdot\mathbf{C}) - \mathbf{C}(\mathbf{A}\cdot\mathbf{B})$ and Eq. (2.1) and (2.2), the wave equation can be obtained by

$$\nabla^2 \mathbf{E} - \varepsilon\mu_0 \frac{\partial^2 \mathbf{E}}{\partial t^2} = 0 \tag{2.3}$$

Eq. (2.3) represents the propagation of light in linear, lossless and nonmagnetic media. Assuming the electromagnetic wave with an angular frequency, $\omega = \frac{2\pi c}{\lambda}$, the electric field vector **E** can be expressed as

$$\mathbf{E}(\mathbf{r},t) = \mathbf{E}(\mathbf{r})e^{j\omega t} \tag{2.4}$$

Therefore, by substituting Eq. (2.4) into (2.3) and using the relation, $\frac{\partial}{\partial t} = j\omega$, Eq. (2.3) can be rewritten by

$$\nabla^2 \mathbf{E}(\mathbf{r}) + n^2 k_0^2 \mathbf{E}(\mathbf{r}) = 0 \tag{2.5}$$

where $k_0 = \frac{\omega}{\mathrm{c}}$ is the propagation constant in free space, $c = \frac{1}{\sqrt{\mu_0\varepsilon_0}}$ is the light velocity in free space, and $n = \sqrt{\varepsilon_r}$ is the refractive index of the medium.

2.1.2 Surface Plasmon Solutions

Surface plasmons (SPs) are charge density waves that propagate along the surface of metals when an optical wave at an incident excitation angle impinges the metal-dielectric interface. The derivation of SP solution in this section is the summary of reference 51, and reference 52 is referred. The SP modes can be derived from solutions of Maxwell's equations. Since only a *p*-polarized electric field can create the SP mode in the metal, we just focus on a plane wave with a *p*-polarized electric field. Therefore, considering two materials, each comprising a half-space, where the interface is at z=0, the electric and magnetic fields at two materials are as follows.

$$
\begin{aligned}
E_1 &= \begin{pmatrix} E_{x1} \\ 0 \\ E_{z1} \end{pmatrix} \exp(i[k_{x1}x + k_{z1}z - wt]) \\
E_2 &= \begin{pmatrix} E_{x2} \\ 0 \\ E_{z2} \end{pmatrix} \exp(i[k_{x2}x - k_{z2}z - wt]) \\
H_1 &= \begin{pmatrix} 0 \\ H_{y1} \\ 0 \end{pmatrix} \exp(i[k_{x1}x + k_{z1}z - wt]) \\
H_2 &= \begin{pmatrix} 0 \\ H_{y2} \\ 0 \end{pmatrix} \exp(i[k_{x2}x - k_{z2}z - wt])
\end{aligned}
\tag{2.6}
$$

where 1 and 2 denote the materials existing in either half-space 1 (z>0) or 2 (z<0) respectively. From the continuity condition for the components of E and H parallel to the interface:

$$\begin{aligned} E_{x1} &= E_{x2} \\ H_{y1} &= H_{y2} \\ k_{x1} &= k_{x2} = k_x \end{aligned} \tag{2.7}$$

Using Eq. (2.7), Maxwell equation reduces below:

$$\begin{aligned} k_{z1} H_{y1} &= \frac{\omega}{c} \varepsilon_1 E_{x1} \\ k_{z2} H_{y2} &= -\frac{\omega}{c} \varepsilon_2 E_{x2} \end{aligned} \tag{2.8}$$

From Eq. (2.7) and (2.8), the following relation is induced.

$$\frac{k_{z1}}{k_{z2}} = -\frac{\varepsilon_1}{\varepsilon_2} \tag{2.9}$$

If we assume that the quantities at Eq. (2.9) are real numbers (in fact, they are complex numbers with small imaginary values), Eq. (2.9) requires that one of the two materials should have a positive dielectric constant and the other a negative constant. This means that the surface plasmon is excited at the interface of a metal and dielectric. Since the wavevector k_i is composed of k_{xi} and k_{zi}, the k_{zi} can be expressed as below.

$$k_{zi}^2 = \left|k_i\right|^2 - k_{xi}^2 = (\frac{\omega}{c})^2 \varepsilon_i - k_{xi}^2 \tag{2.10}$$

where i=1, 2

From Eq. (2.9) and (2.10), (2.10) is induced below

$$(\frac{\omega}{c})^2 \varepsilon_1 - k_x^2 = (\frac{\varepsilon_1}{\varepsilon_2})^2 [(\frac{\omega}{c})^2 \varepsilon_2 - k_x^2] \tag{2.11}$$

Finally, we find the plasmonic dispersion relation:

$$k_x = \frac{\omega}{c}\sqrt{\frac{\varepsilon_1\varepsilon_2}{\varepsilon_1+\varepsilon_2}} \tag{2.12}$$

In the real case, the dielectric constant of a metal is complex with a negative real part and a smaller positive imaginary part. Therefore, k_x and k_z are the complex numbers. Due to the imaginary part of wavevectors, the phase term of (2.6) is separated as the below example.[51]

$$\exp(i[\{k_z^{'}+k_z^{''}\}z-\omega t]) = \exp(i[k_z^{'}z-\omega t])\exp(-k_z^{''}z) \tag{2.13}$$

The latter term means physically a wave decaying exponentially along z-axis with the decay length $1/k_z^{''}$. This tells that all the plasmonic field E_x, E_y, and H_y have the evanescent wave characteristics.

Also, the intensity of the SPs along x-axis decreases as $e^{-2k_x^{''}x}$ so that the propagation length of the SPs along x-axis which the intensity decreases to 1/e is $L_i = (2k_x^{''})^{-1}$.[52] For example, L_i is about 22 μm in sliver at λ=510 nm and L_i=500 μm at λ=1.06 μm.

2.1.3 Prism Coupling

From the dispersion relation shown in Fig. 2.1, since the momentum of the surface plasmons always exceed that of the photon in free space, the surface plasmons cannot be excited by the plane waves incident on the interface of metal/dielectric. Therefore, the additional momentum is required in order to excite surface plasmons.

Conventionally, two configurations have been proposed to excite surface plasmons by letting the excitation light pass through a medium with a high refractive index. One is

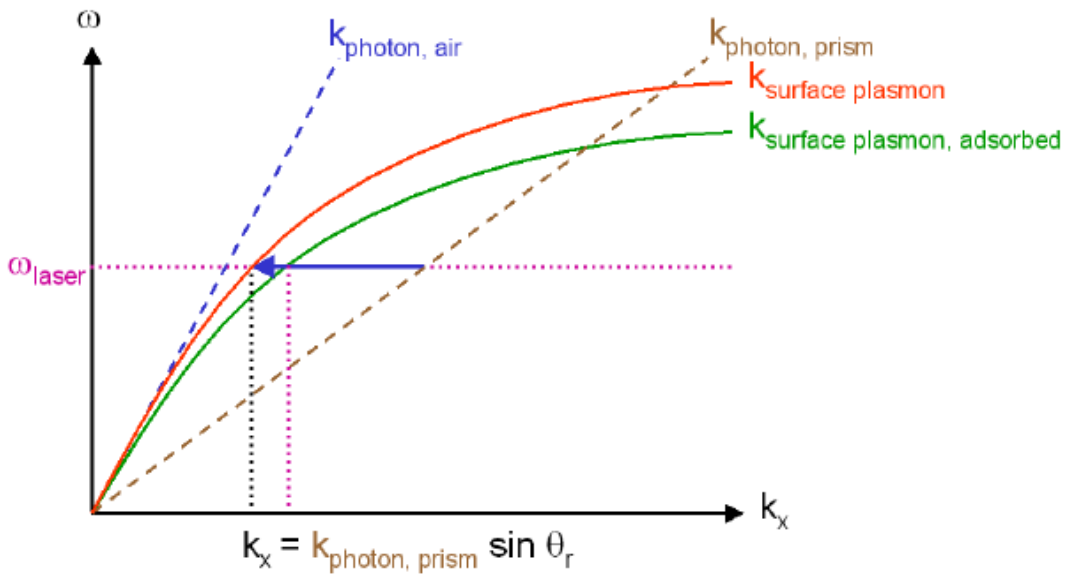

Fig. 2.1 The plasmonic dispersion relation fro prism coupling. Tuning the incident angle can lead photonic k_x to mtacheing the plasmonic in-plane wavevector component, resulting in the excitation of surface plasmons.[51]

Otto configuration that the excitation light comes from the side of dielectric, the other is Kretschmann configuration that the excitation light come from the side of metal as shown in Fig. 2.2. In the Otto configuration, there is a gap of low refractive index material with a thickness of the order of the wavelength of incident beam between the prism and the metal. Under the total internal reflection (TIR) condition which the incident angles equal to or larger than the critical angle, the evanescent field at the prism passes through the low refractive index material such that it excites the surface plasmons

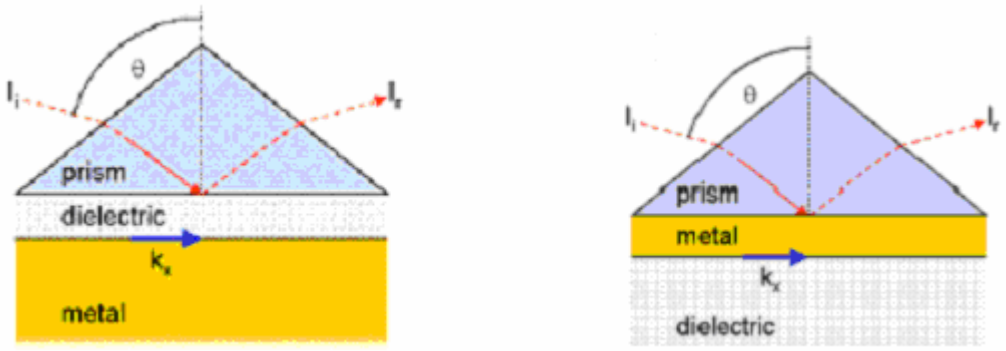

(a) (b)

Fig.2.2 Prism coupling (a) Otto configuration and (b) Kretschmann configuration.[51]

at the interface of metal/dielectric. The Kretschmann configuration is the common method because it offers the simplicity and robustness. Here, a thin metal film is located on the prism and the incident beam is reflected off the prism and the reflected intensity is measured. The metal film should be very thin and precisely controlled because the light field should reach through the film enough to obtain the most efficient coupling to the excitation.

2.1.4 Grating Coupling

Metallic gratings used in monochromators and spectrometers as the dispersive element can be functioned to satisfy the energy and momentum matching condition.[51] A grating is similar to a periodically corrugated surface, therefore, Fig.2.3 shows the simplest grating of the sinusoidal shape. If a plane waves is incident to a metal-dielectric interface with the periodical corrugation, the incident plane wave is diffracted by the

grating functioning as a sort of scattering sources. Then, the momentum of the diffracted waves increases by multiples of the grating wave vector. If the in-plane total component of momentum of a diffracted order matches the plasmon dispersion relation, the plasmons are excited. Therefore, if the corrugated surface of the diffraction grating is oriented perpendicular to the incident plane, the in-plane wavevector of the diffracted waves can be expressed as follows.[51]

$$k_{diffacted} = k_x + mG \tag{2.14}$$

where m is an integer indicating the diffraction order, k_x is the component of the wavevector of the incident light, G is the grating vector which magnitude is $2\pi/\Delta$ (Δ is a grating constant) and $k_{diffracted}$ is the wavevector of the diffracted optical wave. Therefore, the above equation may be expressed as:

$$\pm\sqrt{\frac{\varepsilon_m \varepsilon_d}{\varepsilon_m + \varepsilon_d}} = n_d \sin(\theta) + m\frac{\lambda}{\Delta} \tag{2.15}$$

where θ is the angle of the incident wave, Δ represents a grating constant. When the above equation is satisfied, a SP is excited and propagate along x-axis and decay along the z-axis.

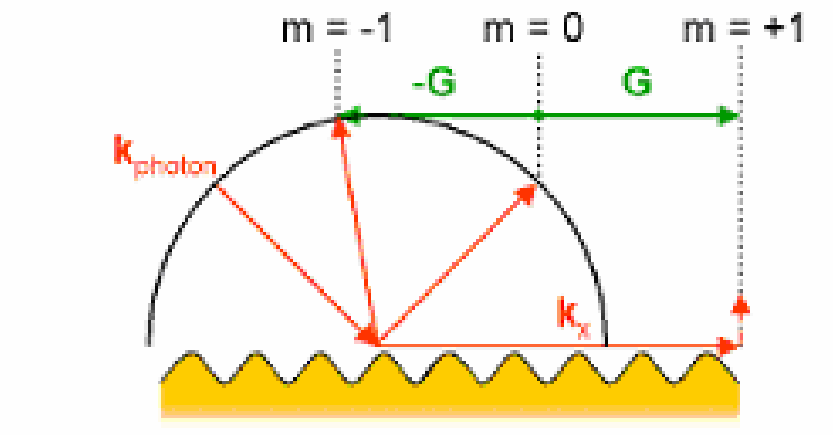

Fig. 2.3 Grating coupling. In the Ewald-like configuration, when the incident waves are diffracted by grating, the incident photon can get the momentum by a factor of multiples of m of the grating vector.[51]

2.1.5 Multi-pass SPR Sensor

To enhance the sensitivity, Su *et al* developed a fiber optic multipass SPR technique that increased the sensitivity by increasing the number of time the light beam travel through the SPR device. The sensitivity enhancement factor is proportional to the number of pass. Since chapters III and IV in this dissertation is based on the multi-pass SPR sensor developed by Su *et al,* in this section, Su's paper[20] is introduced and summarized.

Let's first discuss the theoretical concept for the improved sensitivity of the multipass SPR. Sitting at a bias angle at θ_0 below the resonant angle, the detection power is $P_1=aR(\theta)$ for one pass, and is $P_n=bR_n(\theta)$ for n pass. For a fair comparison, it is assumed that the bias power for the n pass is equal to that of one pass i.e.,

$aR(\theta_0)=bRn(\theta_0) \equiv P_0$. Taking derivatives with respect to θ, the below equations are derived for the one and n passes.

$$\frac{dP_1}{d\theta} = P_0\{\frac{1}{R(\theta_0)}\frac{dR}{d\theta}\}$$
$$\frac{dP_n}{d\theta} = nP_0\{\frac{1}{R(\theta_0)}\frac{dR}{d\theta}\} = n\frac{dP_1}{d\theta} \quad (2.16)$$

Therefore, from Eq. (2.16), we verify that at any bias level, $dP_n/d\theta$ is intrinsically greater than $dP_1/d\theta$ by a factor n, the number of passes.

Fig. 2.4 shows the multipass SPR device setup. It is composed of the right-angle prism, the fiber optic collimator/reflector unit, and a corner cube prism. In brief, the operation principle is as follows. Once the collimator delivers an optical beam to the substrate, the optical beam is reflected by Au surface, then it propagates toward the corner cube. The beam is reflected by the corner cube, which hits the gold surface the second time and proceeds towards the reflector. The backward reflected light from the reflector retraces the previous light path, eventually the beam return back into the collimator after hitting the gold surface four times.

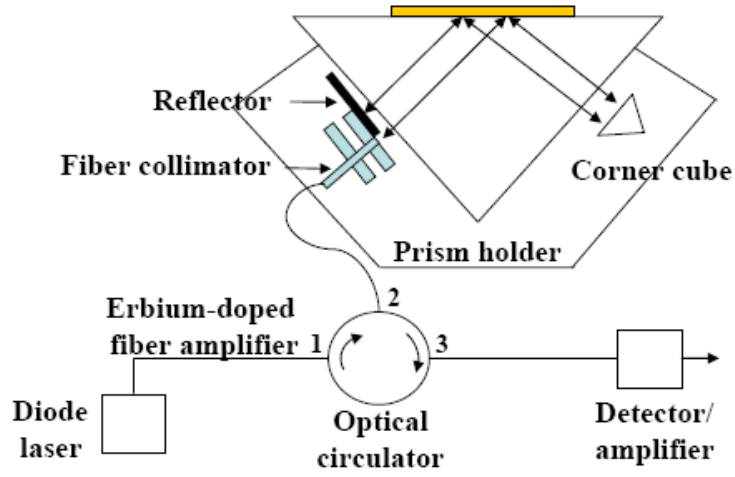

Fig. 2.4 Surface plasmon resonance device with a fiber coupler implemented to inject and detect light.[20]

In order to increase the number of passes beyond 4, pulse operation of the laser light is needed. The concept of increasing the number of passes beyond four is illustrated in Fig. 2.5. The initial input optical pulse driven by a pulse generator enters the optical circulator via the EDFA, then into the SPR device. Then the returning pulse from the SPR having four passes configuration is again propagated into the same EDFA through a fiber splitter.

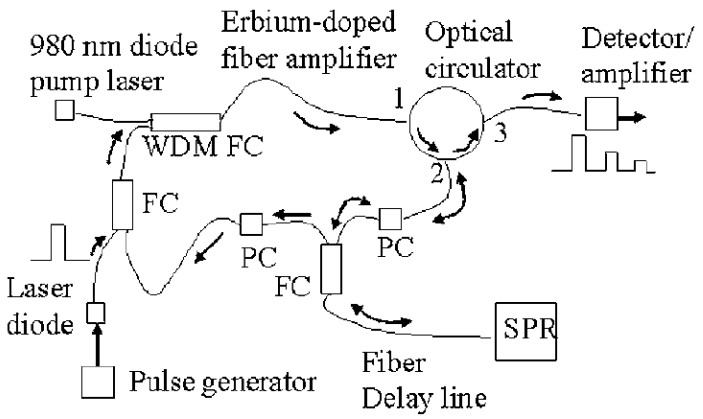

Fig. 2.5 Fiber optic configuration for increasing the number of passes beyond 4. All pulses exit the circulator by port 3. Arrows show the optical path of the recirculating pulses starting from the pulse emitted by the diode laser. FC: fiber coupler. PC: polarization controller.[20]

It creates another set of four passes through the gold surface, therefore, the total number of passes has increased to 8. Theoretically, the number of passes can be infinite. A fiber delay line separates the individual pulses. All pulses entering the SPR are the TM polarized waves by the polarization controller.

Fig. 2.6 shows a log plot of the reflectivity versus the angle for the case of one, four and eight passes through the gold surface. The measured minimum reflectvities are about (0.5 and 0.13)$\times 10^{-2}$ for the case of one and four passes. For eight passes, the power level at minimum reflectivity is below the detectable limit (0.04 mV).

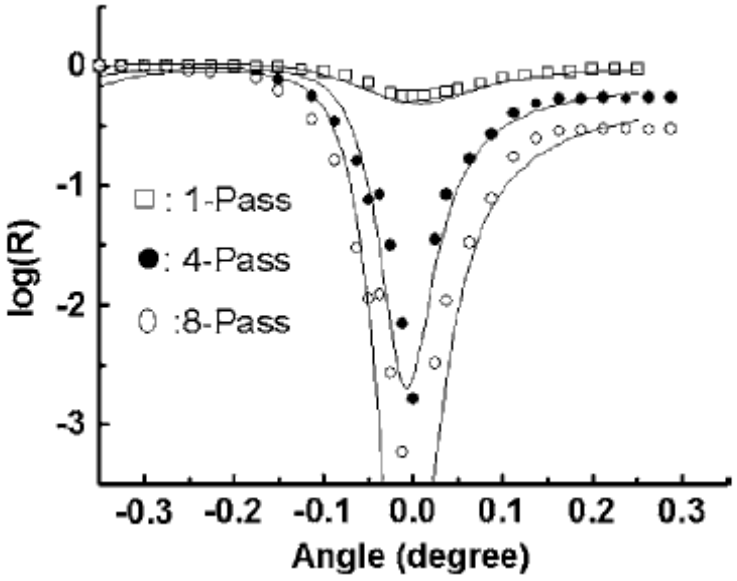

Fig. 2.6 Log plots of the reflectivity vs angle for one, four and eight passes. The points are the measurement data and the lines are calculated curves. 0° represents the resonant angle at 42.02° for the case of Au-air interface.[20]

2.2 Plasmonic Lens

2.2.1 Focusing Light in a Diffraction System

The diffraction limit is the fundamental problem for the spatial resolution in the far field region, which can not be improved instrumentally. In order to explain the maximum spatial frequency briefly, let's begin with Maxwell's equations in differential form. This section is the summary based on references 53 and 54.

$$\nabla \times E = -\mu \frac{dH}{dt}$$
$$\nabla \times H = J_f + \frac{dD}{dt} \qquad (2.17a)$$

where J_f is the free currents. Since the magnetic responses and the free currents can be ignored at optical frequencies, assuming the homogenous, isotropic and linear media, the simplified wave equation is induced as below:

$$-\nabla^2 E = \frac{n^2\omega^2}{c^2} E \tag{2.17b}$$

where n is the refractive index of medium at the imaging plane. The electric field is decomposed into the set of the spatial frequency, k_i in the direction i.

$$\begin{aligned} k_x^2 + k_y^2 +_z^2 &= \frac{n^2\omega^2}{c^2} \\ k_i &\le \frac{n\omega}{c} = \frac{2\pi n}{\lambda_0} \end{aligned} \tag{2.18}$$

This set the fundamental spatial frequency that can be achieved at the conventional optics.

In the regime of Fraunhoffer diffraction, a circular lens as the focusing element limits the focal spot size. The lens creates an Airy disk in the image plane which sized is limited to a minimum diameter of 1.22 λ_0/NA, where NA denotes the numerical aperture defined as $nsin(\theta)$. Where θ is the half-angle of the maximum cone of light that light is collected at the imaging system. Similarly, the minimum resolvable pitch size is set to 0.65 λ_0. Therefore, it is clear that the focal spot smaller than half of wavelength cannot be created in the conventional optic system.

To create the enhanced spatial frequency that overcome the diffraction limit, the use of evanescent waves have been proposed. This evanescent wave has different characteristics with the propagating wave. Assuming that medium is air, the spatial frequency of the evanescent waves in the transverse dimensions, p_x is much greater than

$1/\lambda$. And the intensity of the wave decays exponentially in the longitudinal direction (z-direction), therefore, p_z is imaginary. Therefore, for and the momentum conservation lead to the following relation.[54]

$$\sqrt{p_x^2 + p_z^2} = 1/\lambda \tag{2.19}$$

Since $p_x >> 1/\lambda$, the above equation results in $p_z \approx j p_x$ This indicates that the evanescent wave is effective only within a distance of $\sim 1/p_x$, that is to say, about a distance comparable to a fraction of wavelength. This means that the high spatial resolution beyond diffraction limit exist in the near field region as shown in Fig. 2.7. Assuming that the optical beam is incident through the metal plate with a very small aperture which aperture size, w is much smaller than the incident beam wavelength, λ, the field below the metal plate just results from the small aperture, because the metal plate block the all beam path except the small aperture. Due to the very small aperture size, the high spatial resolution can be achieved, moreover, the resolution can be improved by decreasing the aperture size.

Although the much smaller aperture than incident wavelength can create the high resolution beyond the diffraction limit, this resolution can be achieved in the near field, that is, only within the distance of a fraction of wavelength from the aperture. This cause troubles for the real applications. First, the light transmission efficiency is extremely low. Secondly, for the real application into the microscopy, lithography, etc, the control of the working distance between aperture and sample is not trivial. Thirdly, due to the small working distance and low transmission efficiency, the scanning speed might be very low and the contrast might be poor.[54]

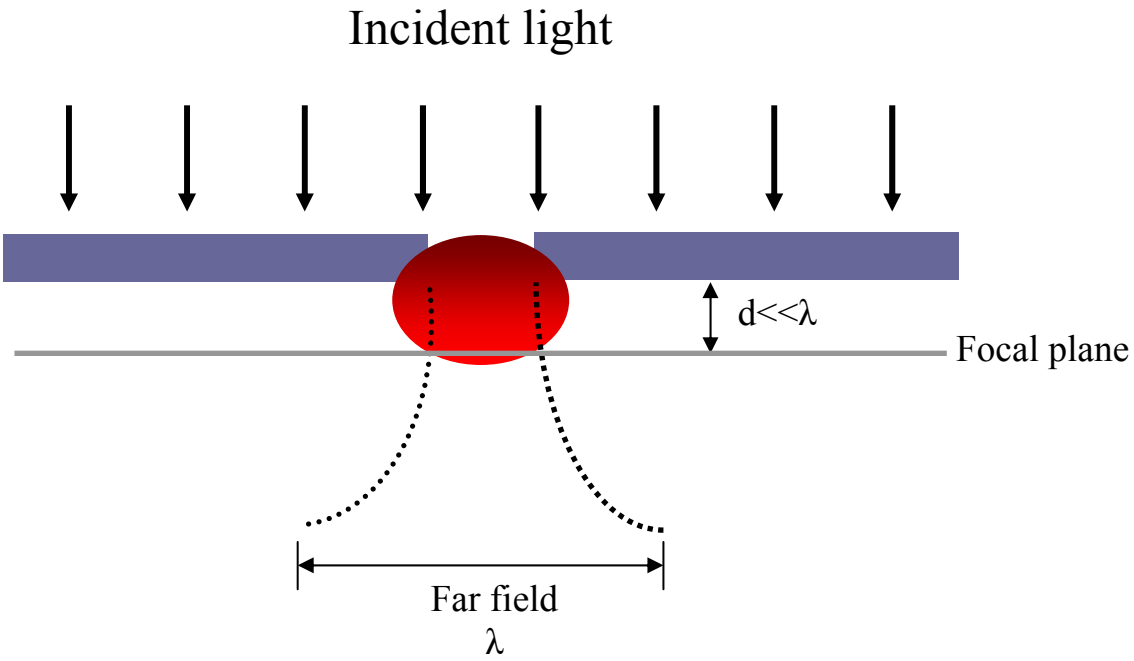

Fig. 2.7 The basic features of sub-wavelength resolution in near field optics.[54]

2.2.2 Optical Constants of Metals and Dielectric

Since the dielectric constant *ε(w)* means the macroscopic response of a material to electromagnetic waves, *ε(w)* for the metals and dielectric in the visible range should be understood. In dielectric, the electrons are strongly bounded to the atomic sites, therefore, as shown in Fig. 2.8(a), in the visible range, the real part (ε') of the dielectric constant generally has the small positive value whereas its imaginary part (ε'') is almost zero.[51]

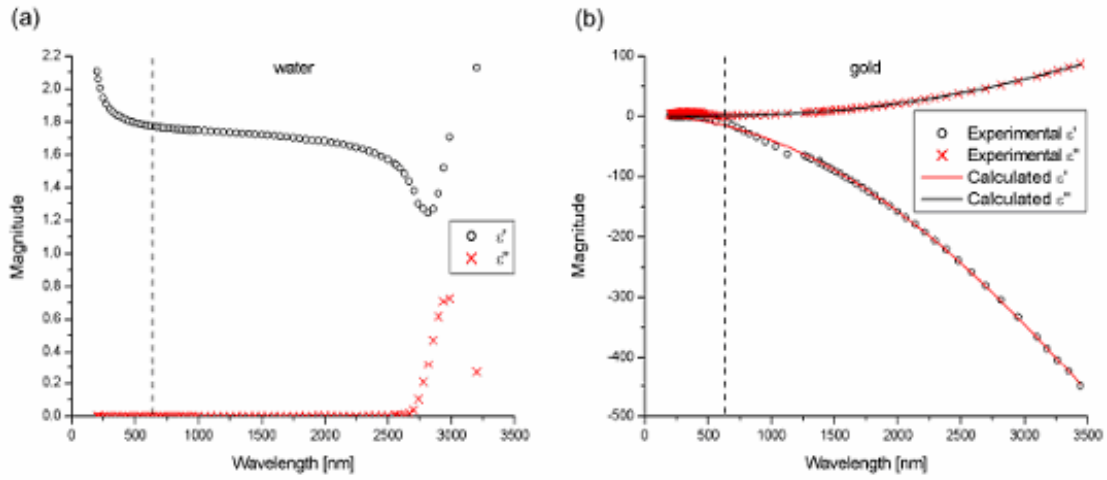

Fig. 2.8 Dielectric functions of water and gold.[51]

Metal has the free-electron that can move freely in between different lattice sites such that in an external filed, the electrons can be accelerated. The free motion of electrons causes the collision with the lattice sites with the collision time τ, which results in the loss of directional information. Generally, in the visible and infra-red ranges, metal has a negative ε' and positive ε'', especially, $|\varepsilon'| \rangle\rangle |\varepsilon''|$ (Fig. 2.8(b)). The dielectric properties of metals were developed by Drude. The frequency dependent dielectric constant ε(w) of metals called Drude model is as below.

$$\varepsilon(\omega) = \varepsilon(\infty) - \frac{\omega_p^2}{\omega(\omega + i\gamma_0)} \approx \varepsilon(\infty) - \frac{\omega_p^2}{\omega^2} + i\frac{\gamma_0 \omega_p^2}{\omega^3} \qquad (2.20)$$

where ω_p is the plasma frequency, γ_0 is the electron relaxation rate. And $\varepsilon(\infty)$ represents the contribution of the bound electrons to polarizability, so, if we assume that the

contribution of the bound electrons is ignored, ε(∞) equals 1. The plasma frequency, ω_p and the electron relaxation rate, γ_0 are given by

$$\omega_p^2 = \frac{n_e e^2}{\varepsilon_0 m_e} \tag{2.21a}$$

$$\gamma_0 = \frac{ne^2}{\sigma m_e} \tag{2.21b}$$

where n_e, e and m_e is the density, charge and effective mass of electrons, respectively. And, σ denotes the DC conductivity. (The section is quoted from references 51 and 55)

2.2.3 FDTD Simulation

The numerical simulation of the nanostructure plasmonic lens is calculated with the finite difference time-domain (FDTD) method. The FDTD method was first developed by Kang Yee in 1966 [56] and it is a numerical method for solving Maxwell's differential equations with the finite differences in time and space, whereas the rigorous coupled wave analysis (RCWA) method is a frequency domain numerical method which decomposes the geometry into spatial frequency domain. Although the RCWA is a good simulation tool for the periodic grating structure, it is not useful for the complicated geometry [57]. Therefore, for the study of subwavelength optics such as 2D aperture or cylindrical ring structure, the FDTD method is generally used. Here, the Yee's paper reported in 1966 is summarized briefly.

Since the FDTD method is to solve Maxwell's equations rigorously, the FDTD algorithm is based on solving Eq. 2.22 numerically using central differences.

$$-\frac{\partial B_x}{\partial t} = \frac{\partial E_z}{\partial y} - \frac{\partial E_y}{\partial z} \tag{2.22a}$$

$$-\frac{\partial B_y}{\partial t} = \frac{\partial E_x}{\partial z} - \frac{\partial E_z}{\partial x} \tag{2.22b}$$

$$\frac{\partial B_z}{\partial t} = \frac{\partial E_x}{\partial y} - \frac{\partial E_y}{\partial x} \tag{2.22c}$$

$$\frac{\partial D_x}{\partial t} = \frac{\partial H_z}{\partial y} - \frac{\partial H_y}{\partial z} - J_x \tag{2.22d}$$

$$\frac{\partial D_y}{\partial t} = \frac{\partial H_x}{\partial z} - \frac{\partial H_z}{\partial x} - J_y \tag{2.22e}$$

$$\frac{\partial D_z}{\partial t} = \frac{\partial H_y}{\partial x} - \frac{\partial H_x}{\partial y} - J_z \tag{2.22f}$$

Let us denote a grid point of the space as $(i, j, k) = (i\Delta x, j\Delta y, k\Delta z)$ and for any functions put $F^n(i\Delta x, j\Delta y, k\Delta z, n\Delta t) = F^n(i, j, k)$. In the following, a set of finite difference equations for the above equations are derived as follows.

The finite difference equation for Eq. 2.22a is

$$\begin{aligned}&\frac{B_x^{n+1/2}(i, j+1/2, k+1/2) - B_x^{n-1/2}(i, j+1/2, k+1/2)}{\Delta t} \\ &= \frac{E_y^n(i, j+1/2, k+1) - E_y^n(i, j+1/2, k)}{\Delta z} - \frac{E_z^n(i, j+1, k+1/2) - E_z^n(i, j, k+1/2)}{\Delta y}\end{aligned} \tag{2.23}$$

Similarly, the finite difference equations for Eq. 2.22b and 2.22c are derived.

The finite difference equation for Eq. 2.22d is

$$\begin{aligned}&\frac{D_x^n(i+1/2,j,k)-D_x^{n-1}(i+1/2,j,k)}{\Delta t}\\&=\frac{H_z^{n-1/2}(i+1/2,j+1/2,k)-H_z^{n-1/2}(i+1/2,j-1/2,k)}{\Delta y}\\&-\frac{H_y^{n-1/2}(i+1/2,j,k+1/2)-H_y^{n-1/2}(i+1/2,j,k-1/2)}{\Delta z}+J_x^{n-1/2}(i+1/2,j,k)\end{aligned} \tag{2.24}$$

Also, the equations for 2.22e and 2.22f can be similarly derived. Fig. 2.9 shows the Yee unit cell that describe the grid points for the E-field and the H-field, where every E component is surrounded by four H components and vice versa.

The grid size should be as small as the electromagnetic field does not change significantly over one increment. Therefore, for constant ε and μ, the computational stability should be satisfied by the Cournat condition as follows.[54]

$$\sqrt{(\Delta x)^2+(\Delta y)^2+(\Delta z)^2}>c\Delta t=\sqrt{\frac{1}{\varepsilon\mu}}\Delta t \tag{2.25}$$

where Δx, Δy, Δz are the grid sizes, Δt is the time step size and c is the velocity of light. Therefore, Δt is limited for the chosen Δx, Δy and Δz.

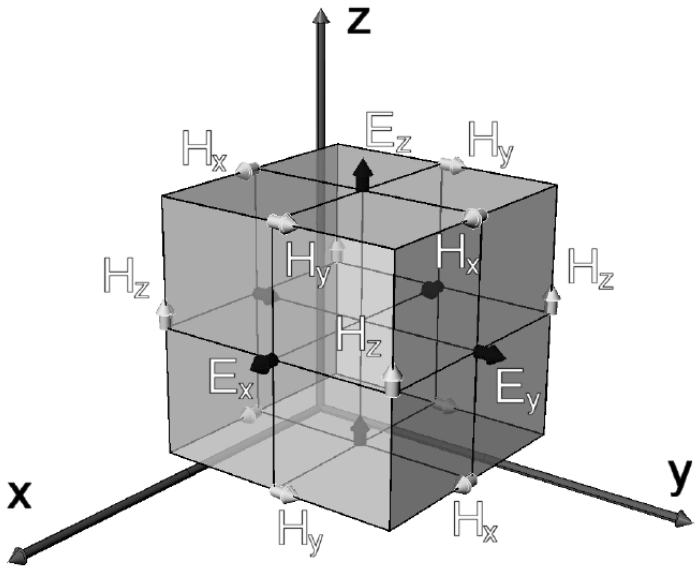

Fig. 2.9 Position of the electric (black arrows) and magnetic (white arrows) field vector components of the Yee cell.[57]

In addition to the solution from Eq.2.22, it is necessary to consider boundary conditions in order to calculate the grid to infinity and remove non-physical reflections. For this boundary conditions, perfect matched layer (PML) is used.[57] The PML is a non-physical anisotropic material which can absorb incident radiation from various angles without reflection. This is accomplished by allowing the wave impedance to be equal at both sides of the surface.[57]

$$\eta_1 = \sqrt{\frac{\mu_1}{\varepsilon_1}} = \sqrt{\frac{\mu_{PML}}{\varepsilon_{PML}}} = \eta_{PML} \tag{2.26}$$

Fig. 2.10 shows a example of the boundary condition of simulation domain that is used in this study.

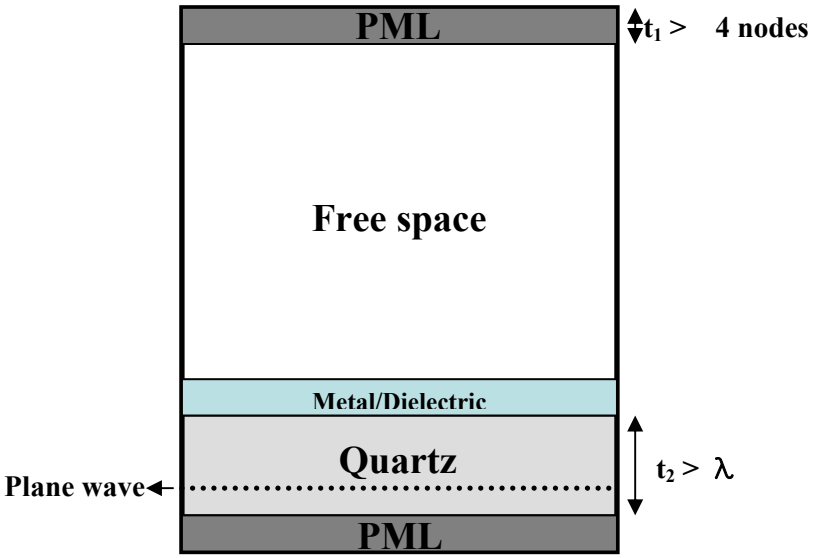

Fig. 2.10 Schematics for the boundary condition of simulation domain.

2.2.4 Metallic SP Lens

Recently, Sun *et al.*[30] reported the refractive transmission of light through a metallic nanoslit array and demonstrated beam shaping functions of the convex-shaped metallic lenses. They mentioned that the metallic nano slit lens do not suffer from a strong diffraction effect at lens edges while the conventional dielectric lenses have the edge effect. Moreover, they verified that the phase of each nanoslit element can be controlled by adjusting structural and materials parameters such as slit width and the dielectric constant in the slit region. Also, Yuan *et al.* reported the principle and design

approach of the metallic SP lens. So, in this section, the design and basis of the SP lens that have been studied by Yuan *el al.* [36] is introduced and summarized.

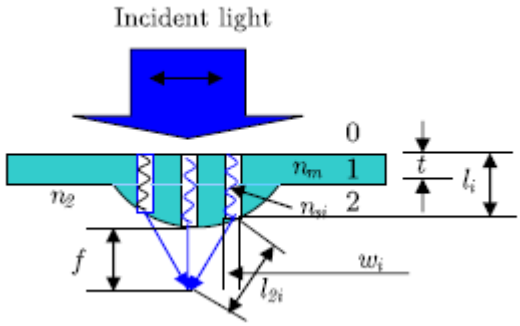

Fig. 2.11 Schematic of the refractive SP lens.[36]

Fig. 2.11 shows the schematic of a refractive metallic SP lens. A universal relationship among the geometrical parameters and focal length is obtained below:

$$k_0(n_{si}l_i + n_2 l_{2i}) - k_0(n_c l_c + n_2 f) = 2m\pi \tag{2.27}$$

where n_{si} is the equivalent refractive index inside the slit for the working wavelength, l_i is the *i*th slit length, n_c is the equivalent refractive index at the central slit, l_c is the slit length at the central slit and f is the back focal length. This will be rewritten as

$$(n_{si}l_i + n_2 l_{2i}) - (n_c l_c + n_2 f) = m\lambda_0 \tag{2.28}$$

Since the equivalent refractive index is a function of the effective wave number in the slit, β, the SP symmetrical modes for an infinite metal slit with TM incidence should be considered.

$$\frac{k_0 w}{2}\sqrt{\varepsilon_s - (\frac{\beta}{k_0})^2}\ \tan[\frac{k_0 w}{2}\sqrt{\varepsilon_s - (\frac{\beta}{k_0})^2}\,] = \frac{\varepsilon_s}{\varepsilon_m}\frac{k_0 w}{2}\sqrt{(\frac{\beta}{k_0})^2 - \varepsilon_m} \tag{2.29}$$

where ε_s is the dielectric permittivity of the material inside the slit, ε_m is the dielectric permittivity of the metal film. Therefore, from, the eq xx, β can be derived, so the equivalent refractive index for each slit can be derived as

$$n_{si} = \frac{\beta_i}{k_0} \tag{2.30}$$

Therefore, the equivalent refractive index in slit is a function of slit width, length.

Considering the finite slit length in a refractive SP lens, the transmittance with respect to slit length is given as

$$t_i = \frac{t_{01} t_{12} e^{j\beta l_i}}{1 + r_{01} r_{12} e^{2j\beta l_i}} \tag{2.31}$$

where the subscripts 0,1 and 2 represent the media before, inside, and after the nano-slit array, respectively. And the transmittance at the interfaces t_{01} and t_{12} can be expressed by

$$t_{01} = 1 - \frac{n_0 - n_{si}}{n_0 + n_{si}} \tag{2.32}$$

$$t_{12} = 1 - \frac{n_{si} - n_2}{n_{si} + n_2} \tag{2.33}$$

Fig. 2.12 shows the transmission as a function of slit length and width. It indicates that different phase retardations can be achieved by designing both slit length and slit width and pitch as well.

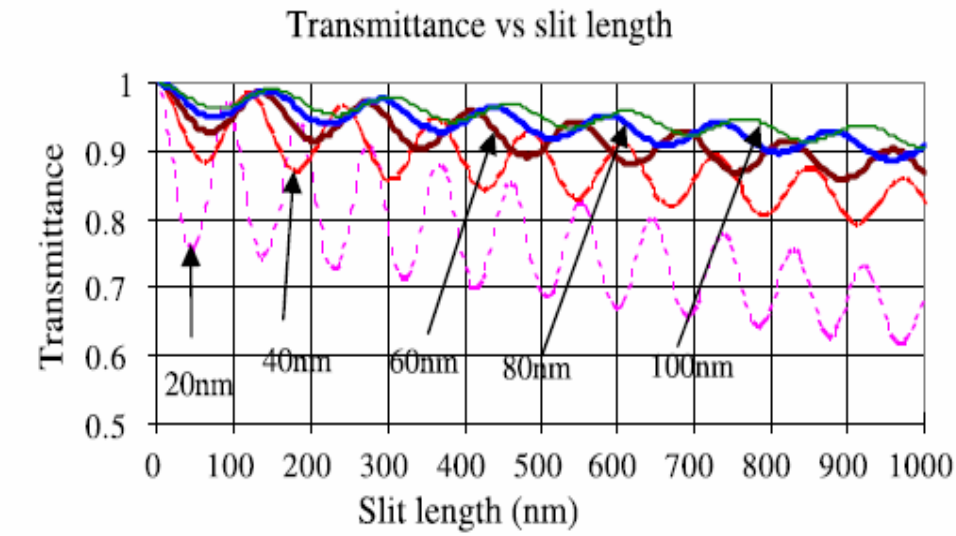

(a)

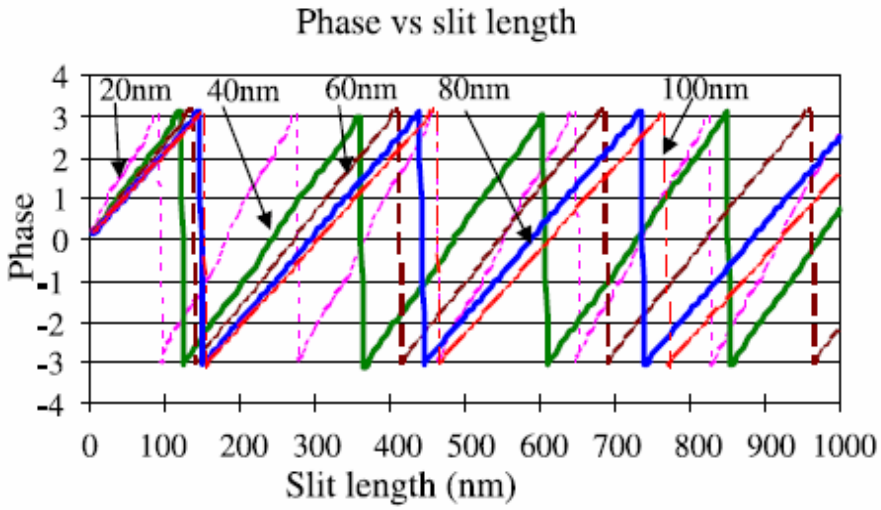

(b)

Fig. 2.12 Variation of transmission with slit length up to 1μm. Media 0, 2, and the material inside the slit are air. Working wavelength is 400 nm. The effect of the slit is also shown in different data series. (a) Amplitude of transmittance vs. slit length, (b) phase of transmittance vs. slit length.[36]

However, the fabrication of the lens shown in Fig. 2.12 is a big challenge in practice. Therefore, the flat metallic SP lens is desired as shown in Fig. 2.13. It shows the flat nano-metallic SP lens with variable slit width but fixed pitch for each slit. Eq. 2.28 can be customized as

$$[n_{si}t + n_2\sqrt{f^2 + (ip)^2}] - (n_c t + n_2 f) = m\lambda_0 \tag{2.34}$$

where t is thickness of the Ag film and p is pitch. Once the desired focal length f is fixed, the slit width can be obtained from Eq. 2.29.

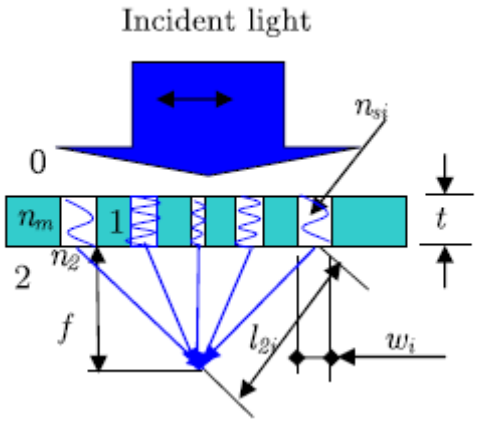

Fig. 2.13 Schematic of the flat nano-metallic SP lens with variable slit width but fixed pitch for each slit.[36]

2.2.5 Cut-off Wavelength for Subwavelength Hole in a Real Metal

To understand the light transmission in subwavelength structure, we first need to understand cut-off condition that no propagation of light exist. In perfect metal, the cut-off condition occurs when the wavelength is greater than twice hole size. However, Gordon *et al.* [31] reported the numerical calculation that the Ralyleigh's cut-off condition is increased significantly for real metals. In this section, to understand the propagation mode of light through subwavelength structure in real metal, Gordon's article is summarized.

Fig. 2.14 shows the geometry of hollow rectangular waveguide in a metal. They explained the extended cut-off wavelength due to two factors, that is, one is penetration of the field into the metal along the x-direction, and the other is coupling between SP modes along the y-direction as following.

Firstly, the cut-off increase from penetration of the electric field into the metal is explained as follows. In the case of a perfect electric conductor (PEC), the propagation constant of the TE_{01} mode of a rectangular hole is

$$\beta = \pi\sqrt{(\frac{2}{\lambda})^2 - (\frac{1}{a})^2} \tag{2.35}$$

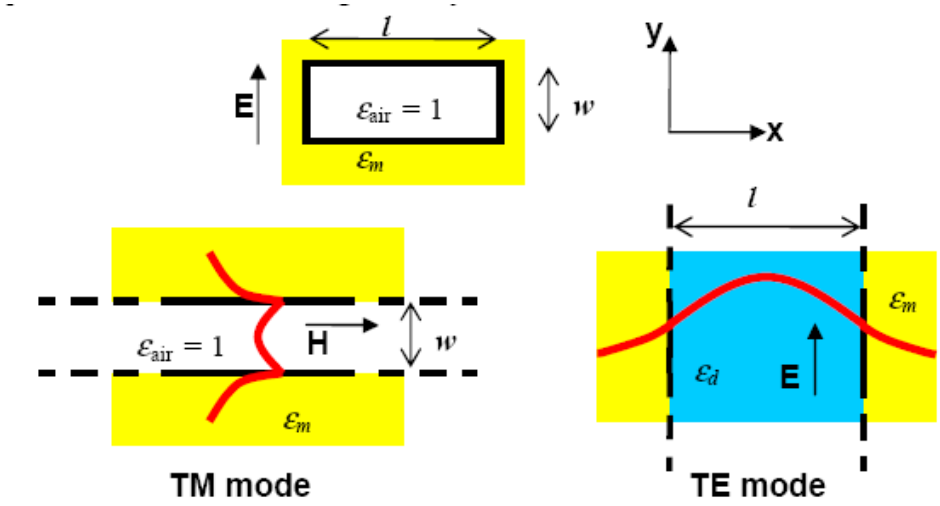

Fig. 2.14 Schematic of hollow rectangular waveguide in a metal, with co-ordinates shown. The lowest-order mode is analyzed by considering the TM moded of a slab of sidth *w*, to derive an effective dielectric constant, and then solving for the TE mode component in a slab of separation *l* filled with the effective dielectric. This provides the effective dielectric constant for the lowest-order mode of the rectangular waveguide.[31]

where a is the length of the rectangle and λ is the wavelength of light. The cut-off wavelength is a condition that the propagation constant of the TE_{01} mode is zero, that is, $\lambda = 2a$.

In real metals, the metal's relative permittivity has a negative real part and a small imaginary part. The electric field can penetrate into the metal by the skin-depth, making the hole appear larger. Therefore, the propagation constant of a TE mode between two parallel plates of a real metal, β_{TE} is found as below.

$$\tan(\sqrt{k_0{}^2\varepsilon_d - \beta_{TE}^2}\, l/2) = \frac{\sqrt{\beta^2 - k_0^2\varepsilon_m}}{\sqrt{k_0{}^2\varepsilon_d - \beta_{TE}^2}} \tag{2.36}$$

where ε_m is the relative permittivity of the metal, and ε_d is the relative permittivity of the dielectric between the metal sides, l is the length between the metal sides and $k_0 = 2\pi/\lambda$ is the free-space wave-vector. Therefore, the cut-off wavelength can be obtained below, at which β_{TE} is equal to zero.

$$\lambda_{cut-off} = \frac{\pi d\sqrt{\varepsilon_d}}{\arctan\sqrt{-\varepsilon_m\varepsilon_d}} \tag{2.37}$$

Secondly, the cut-off wavelength increases as the hole size become smaller due to the coupled SP waves. Let's consider the two parallel plates in order to derive the TM mode that results from the sum of SP modes of top and bottom plates. The field between the plates is the sum of two exponentially decaying SP modes on the top and bottom. . The propagation constant β_{TM} can be calculated from the below equation.[19]

$$\tanh(\sqrt{\beta_{TM}{}^2 - k_0^2\varepsilon_d}\, w/2) = \frac{-\varepsilon_d\sqrt{\beta_{TM}{}^2 - k_0^2\varepsilon_m}}{\varepsilon_m\sqrt{\beta_{TM}{}^2 - k_0^2\varepsilon_d}} \tag{2.38}$$

For example, for a 105 nm aperture in silver at 750 nm of wavelength, the β_{TM} is $1.2\,k_0$. Therefore, the effective refractive index, β_{TM}/k_0 is 1.2. Moreover, the effective index increases critically as the width of the hole is reduced. Therefore, by reducing the hole size, the SP-mode coupling increases so that the cut-off wavelength increases significantly.

CHAPTER III

A FIELD-ASSIST FOUR-PASS FIBER OPTIC SURFACE PLASMON RESONANCE SENSOR

3.1 Experiments

Fig. 3.1 shows the original multi-pass fiber optic SPR sensor system with the addition of a field-assist method. The principle and properties of a multi-pass SPR system were described in reference 20. In brief, the incident optical beam from the fiber collimator propagates toward the corner cube after the first reflection off the gold surface. The retro-reflected beam from the corner cube hits the gold surface the second time and proceeds towards the mirror reflector. The retro-reflected beam is exactly parallel to the incident beam (within 2 arc-second). The normal to the reflector is engineered parallel to the beam emanating from the fiber collimator. The beam reflected by the mirror exactly retraces the previous light path, returning to the fiber collimator after impinging the gold surface a total of 4 times. Thus, the fiber collimator serves as an emitter and a receiver. The mirror reflector and the fiber collimator are fixed to a common rotating fixture attached to the prism holder. In this study, a light source wavelength of 1.53 μm was used. The plasma resonance characteristics regarding the sharpness of the resonant profile and the resonant angle shift of gold surfaces at 1.5 μm wavelength compared to commonly used wavelengths of 0.67 and 0.85 μm were discussed in reference 20. However, at the long wavelength of 1.53 μm, the vast fiber optic technology developed

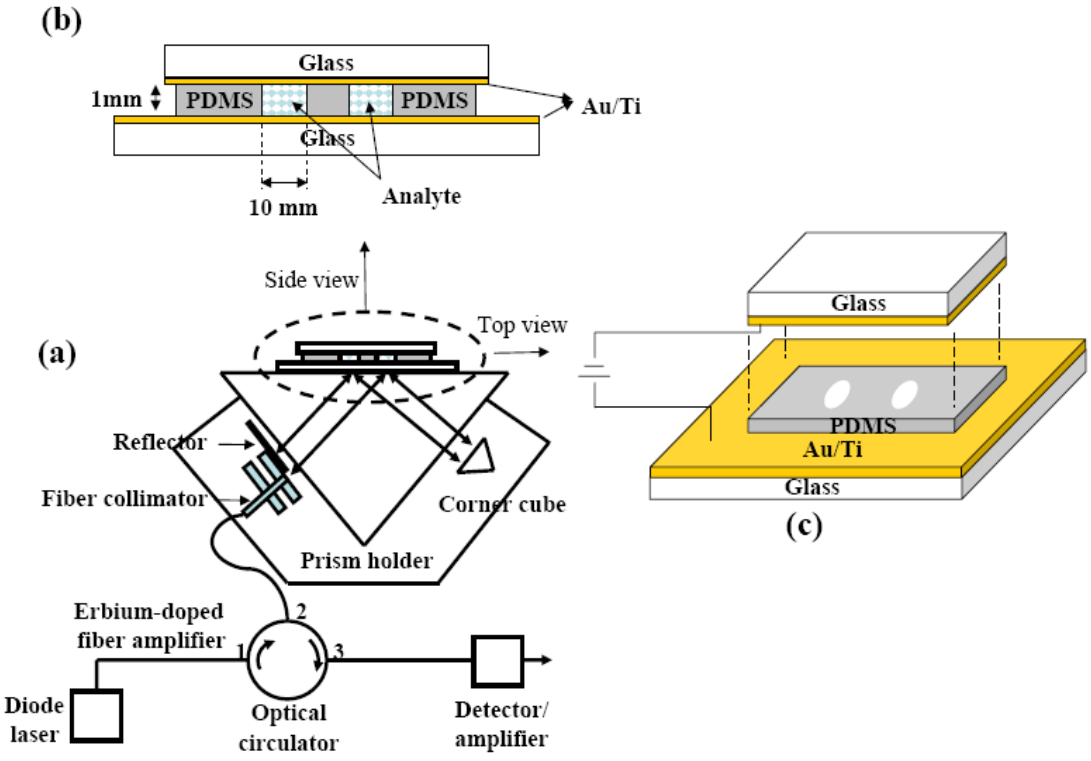

Fig. 3.1 (a) An optical multi-pass SPR sensor system coupled with the field-assist method. (b) Side view of the electrode configuration. (c) Top view of electrode configuration.

for telecommunications applications can be used for building robust and cost-effective SPR sensor.

Two glass wafers with thin gold film on one side of the wafer surface were used. Poly (dimethylsiloxane) (PDMS) sheets are fabricated with two holes that function as solution wells. The gold thin films act as electrodes. The bottom electrode is the SPR surface. The 1 mm thick PDMS sheet is sandwiched between the bottom and top electrodes during measurements as shown in Fig. 3.1(b) and (c). The analyte solution to be measured is dropped into the two holes on the PDMS sheets, and the solution is covered by the top electrode that is electrically grounded with respect to the SPR bottom electrode that is at a positive voltage to collect negatively charge particles onto the SPR surface. The light beam hits the region of the solution well as shown in Fig. 3.1(a).

A 1.53 μm wavelength semiconductor diode laser is used as the light source. The laser can operate in continuous wave or pulse mode. For the data presented below, the laser is under pulse mode operation with a 5 % duty cycle, avoiding the potential of heating the solution by optical absorption. An erbium-doped fiber amplifier (EDFA) amplifies the optical signal from the light source, and the fiber optic circulator delivered the optical signal to the SPR system by routing the amplified signal from port 1 to port 2. The returned signal from the SPR device exit port 3 of the circulator and is detected by a photodetector/amplifier module. The electrical signal is then displayed by a signal processing unit.

Using the Kretschmann's configuration as shown in Fig. 3.2(a), a SPR reflectivity versus incident angle profile is measured and given in Fig. 3.2(b). The reflectivity

exhibits a minimum value at the resonant angle, which for DI water is about 62.6 °. refractive indices of BK-7, Au and DI water at 1.53 were 1.50065, 0.4+9.7i and 1.3159, respectively. A perturbation of the evanescent wave causes a shift in the resonant angle. A shift in the resonant angle towards larger values signifies the presence of a substance with larger refractive index than the background solution's index. If one bias at an angle below the resonance angle (Fig. 3.2(b)), as is the case for all data presented below, the presence of a substance with an effective larger refractive index on the SPR surface will increase the reflected optical power and the detection signal.

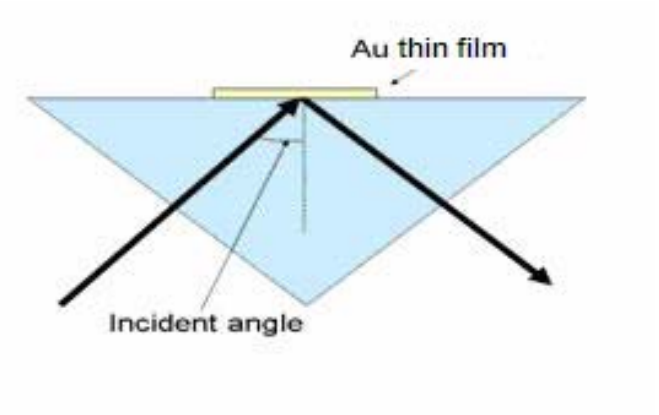

(a)

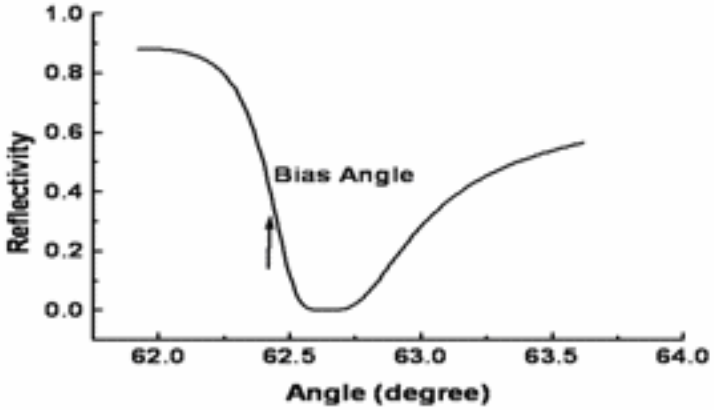

(b)

Fig. 3.2 (a) A schematic drawing that describes the concept of SPR. (b): SPR reflectivity curve as a function of angle. In this experiment the bias angle is set below the resonant angle as depicted.

3.2 Experiment Results

A typical time-dependent SPR signal response to a positive step voltage of 1 and 2 volts applied at time t =0 is shown in Fig. 3.3 for the case of 18 MΩ-cm DI water placed in the solution wells. The increase in SPR signal, and thus the refractive index, is presumably due to the attraction to the SPR surface of the negatively charge OH^- ions, which at a pH of -7 has a concentration of 10^{-7} M. The increase in SPR signal is initially fast and then slows at longer time. This should be due to the build-up of negatively charged particles at the SPR surface, thereby creating an electric field that is opposite in direction to the applied field as prescribed by Gauss law. Thus, the total electric field

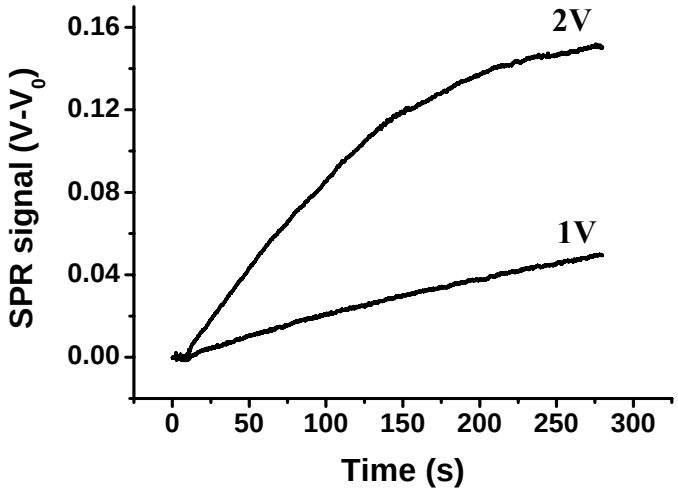

Fig. 3.3 Time-dependent SPR signal of DI water for +1 and +2 volts step-voltage applied across the electrodes at time t = 0. V_0 represents the pulse amplitude before the voltage is applied.

decreases in time, causing a saturation of the SPR signal. The effect of overfilling the evanescent wave region may also be a factor contributing to signal saturations. The larger rate of signal increase at higher applied voltage leads to a quicker saturation of the SPR signal in accordance to the discussion given above.

600 μM ($3.5x10^{-5}$ gram-salt/cc) of salt concentration were prepared. Pulsed signal amplitudes without an applied voltage between the electrodes are compared for three cases. In the first case, the two solution wells are filled with DI water (no salt case). In the second case, one solution well is filled with 600 μM salt solution and the other solution well contains DI water. In the third case, both solution wells are filled with 600 μM of salt solution. Fig. 3.4(a) shows the measured results. The increase in the pulse amplitude is due to an increase of the refractive index of the salt solution over DI water. A rough estimate, using Fig. 3.4(a), indicates that, without an applied voltage, the concentration resolution for salt ions is no better than about 200 μM.

Fig. 3.4(b) shows the results corresponding to the three cases in Fig. 3.4(a), except the salt concentration is diluted to 10 μM and a step voltage of +2 volts is applied across the electrode at time t=0. The amplitude of the pulse is recorded as a function of time. Prior to the turn-on of the step voltage, pulse signal amplitudes for DI water and solution containing 10 μM of salt concentration response are indistinguishable. However with an applied voltage of 2 volts, the response of 10 μM of salt concentration is significantly larger than the response for DI water despite the much lower salt concentration than Fig. 3.4(a). The optical response of salt solutions must be due to the attraction of the negatively charge Cl^- ions to the SPR surface which increase the refractive index at the

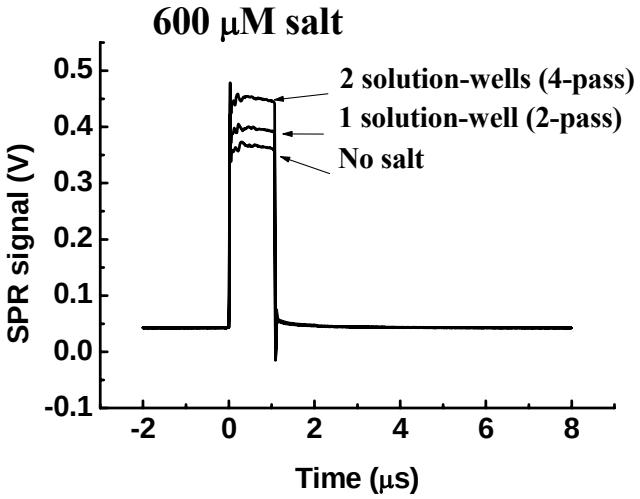

(a)

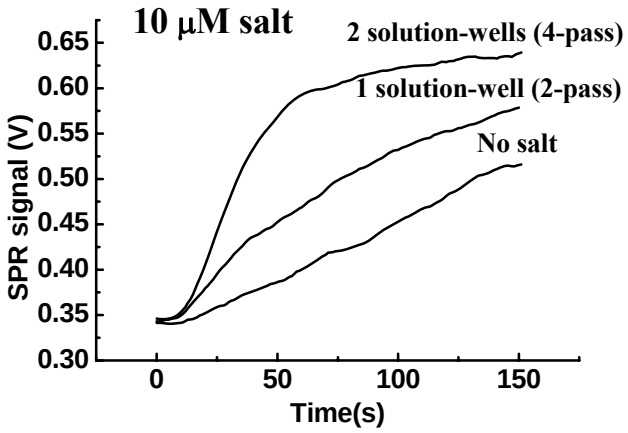

(b)

Fig. 3.4 (a): SPR pulsed signal amplitudes. The salt concentration is 600 μM. No voltage is applied to the electrode. The effective number of multi-pass corresponding to one well and both wells filled with salt solution are two and four respectively. (b): Amplitude of SPR response due to a voltage of +2 volts applied at t =0. The salt concentration is reduced to 10 μM.

SPR region above the index of the background solution.

From Fig. 3.4(b), it is estimated that the minimum detectable salt concentration is about 2 μM, limited by the significant DI water response. The background refractive index, n, of a salt solution is calculated by the formula $n = xn_s+(1-x)n_w$, which is valid for dissolvable substance.[58,59]

Here n_s and x is the refractive index and weight fraction of salt. With $n_s = 1.544$ and $n_w = 1.3159$, 200 μM of salt concentration ($x = 1.2x10^{-5}$ gram-salt/gram water) corresponds to a refractive index increase ($n-n_w$) of $+2.6 \times 10^{-6}$, and 2 μM of salt concentration represents a background refractive index increase of about 2.6×10^{-8} from the refractive index of DI water. Comparing Fig. 3.4(a) and 3.4(b), the concentration resolution improves from about 200 μM to about 2 μM, an improvement of about a factor of 100 with an applied field. This also indicates that the concentrated analyte at the SPR surface amplifies the index change by a factor of 100. Thus, although the background index change is $+2.6 \times 10^{-8}$, the local index change at the SPR surface is $+2.6 \times 10^{-6}$. A temperature monitoring thermistor attached to the glass wafer shows that the temperature does drift continuously upward upon the turn-on of laboratory equipment, but by no more than +0.2 ° C /hour, which amount to a negative refractive index drift of about $-7x10^{-7}$ per two minutes of measuring time, which is not very significant here compare with the local index change of $2.6x10^{-6}$ at the SPR surface.

47 nm diameter polystyrene (PS) were diluted in DI water to a concentrations of 1 nM, 100 pM and 10 pM. The bias angle is arbitrarily fixed at an angle below the resonant angle such that the bias power is 10 times the power at resonance (minimum

reflectivity). Solutions were dropped into the solution wells for measurement. A step voltage of two volts was applied to the electrodes, and the optical response was measured. The response of DI water was first measured and used as a reference signal. Data for DI water and for PS solutions with concentrations of 1 nM, 100 pM and 10 pM are shown in Fig. 3.5. The data initially exhibit a fast response and then slows at longer time, due to similar reasons discussed previously. The data showed that PS beads are negatively charged in DI water solution. The minimum detectable concentration is roughly about 10 pM for a particle size of 47 nm. Comparing with NaCl solution, the larger particle size of PS beads suggests a larger perturbation of the evanescent field than Cl^- ions, thus, a smaller detectable concentration for PS beads than NaCl.

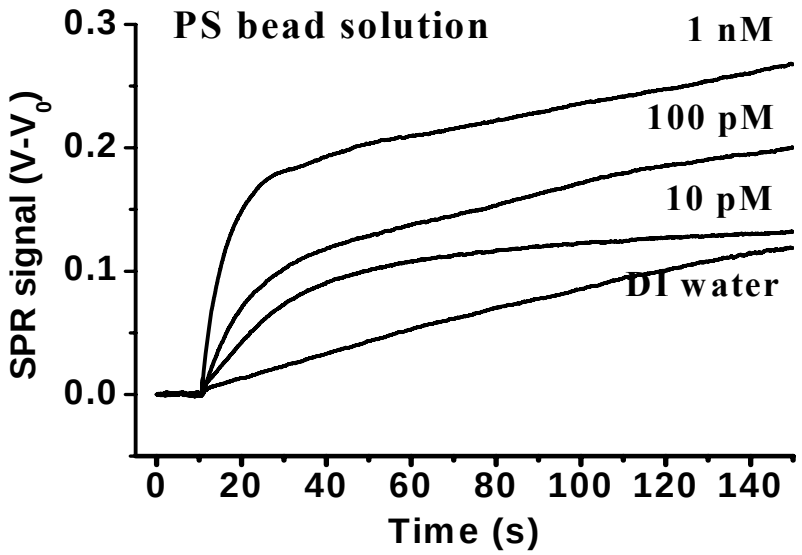

Fig. 3.5 Time-dependent SPR signals for different PS concentrations. The applied voltage is +2V.

Fig. 3.6(a), which is obtained by taking the time-derivative of the signal displayed in Fig. 3.5, suggests that the signal rate increase, dV/dt, is a good measure of charged molecules. This is reasonable because the eventual number of particles that is able to accumulate on the SPR surface depends on the total charge of each particle; ie, the more charge on a particle, the lesser number it can accumulate on the surface due to repulsion of like charge. This repulsion effect is smaller at the initial stage of signal increase. As shown in Fig. 3.6(b), the slope dV/dt, as expected, is a sublinear function of particle concentration because of the charge repulsion effects. An important observation is the fact that charged particles/molecules in the solution can be detected within a few seconds by this method.

When solid particles (not dissolvable in solution) of diameter d and refractive index n_p are dispersed in a liquid of refractive index n_c, the refractive index of the solution can be written as follows.[60]

$$n = n_c + 3\phi(n_p - n_c)(\frac{\sin p}{p^3} - \frac{\cos p}{p^2}) \tag{3.1}$$

where $p = 2\pi d(n_p - n_c)/\lambda_0$. λ_0 is the wavelength and ϕ is the phase volume ratio of the particles. For a bead concentration of 10 pM , $\phi = 3.8\times10^{-7}$. Therefore, according to Eq. 3.1, the index increase $n\text{-}n_c = 9.0\times10^{-8}$, corresponding to the minimum detectable index deviation for the 47 nm diameter PS beads.

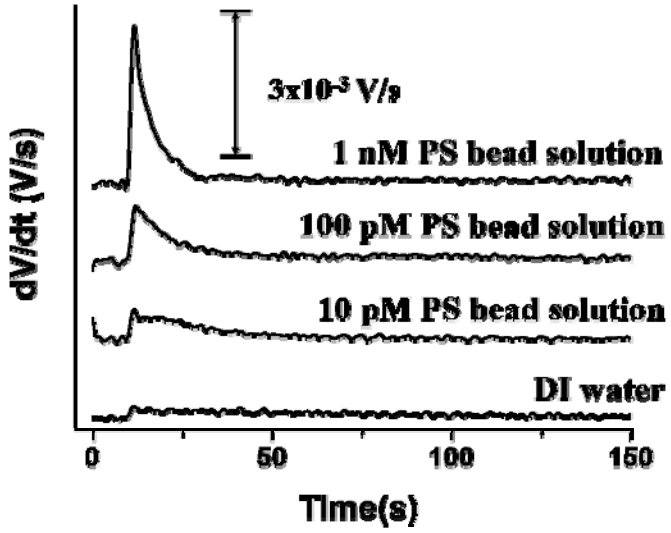

(a)

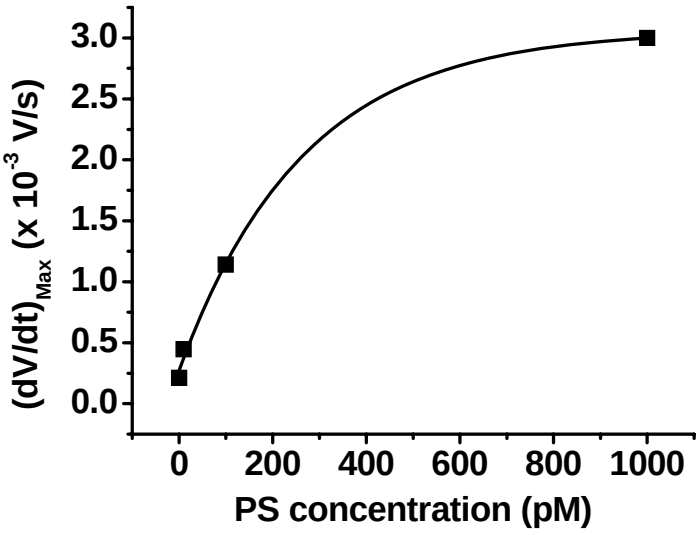

(b)

Fig. 3.6 (a): Time-derivatives of SPR signals of figure 5. (b): A summary of the maximum value of dV/dt as a function of PS concentrations.

3.3 Summary

In summary, a four-pass SPR device with field assist capability to detect charged particles/molecules in a solution is demonstrated. The field assist features have not been reported previously in surface plasmon technology. The sensitivity improvement with an applied voltage is shown. NaCl solution and polystyrene latex beads were used as a test of this technique. For NaCl solution a detectable solute concentration of 2 μM equivalent to an index resolution of 2.6×10^{-8} is shown. 10 pM concentration of 47 nm diameter polystyrene beads can be detected, corresponding to an index resolution of 9×10^{-8}. Another important feature is the rapid detection capability that can be as quick as a few seconds.

CHAPTER IV

FORTY FOUR-PASS FIBER-OPTIC LOOP FOR SURFACE PLASMON RESONANCE SENSOR

4.1 Experiment

Fig. 4.1 shows the SPR system with a practical fiber recirculating loop with the addition of a field-assist method. The principle and properties of the SPR system with the fiber recirculating loop were reported by Su *et al.* [19] In brief, pulse generator 1 drives a laser diode (LD) to create an optical pulse train with about 5% duty cycle and 0.13 μs pulse width. The incident pulse is split into two pulses by fiber coupler 1(FC1). One pulse propagates toward the SPR device by exiting port 2 of the optical circulator and the other is detected by the photodetector (PD) as shown. There are two collimators in the SPR unit. The optical beam exiting port 2 of the circulator is fed to the lower collimator and propagates toward the corner cube on the others side after reflecting off the gold surface. Then, the retro-reflected beam from the corner cube hits the gold surface the second time and returns to the upper collimator. Therefore, the SPR system is a two pass configuration with the lower collimator functioning as a emitter and the upper collimator functioning as a receiver (or vice versa).

The returned optical pulse via the SPR device is reduced in amplitude due to SPR resonance effect and back-coupling loss, therefore, the reduced amplitude needs to be amplified by the erbium-doped fiber amplifier following the electro-optic modulator (EOM). The pulse eventually returns to FC1 after one round trip and the process repeats.

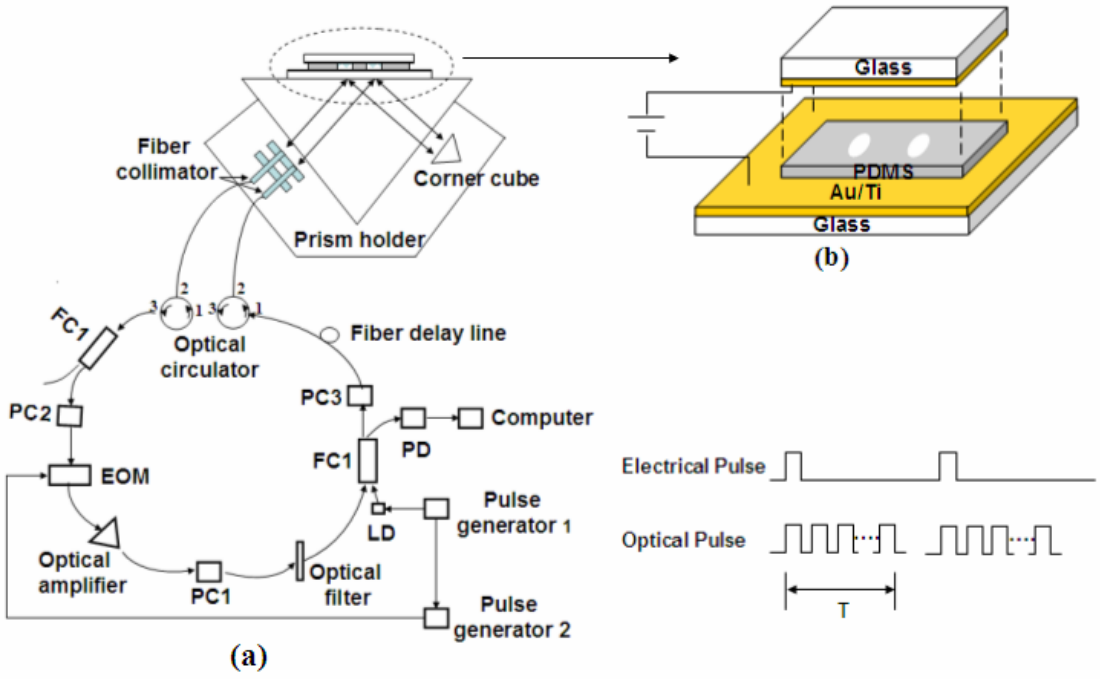

Fig. 4.1 (a) An optical multi-pass SPR sensor system coupled with the field-assist method. Top: SPR , bottom: fiber loop, LD: laser diode, PD: photodiode, PC: polization controller, FC: fiber coupler (b) Side view of the electrode configuration.

Therefore, the detector (PD) detects periodic pulses that are displayed on a digital oscilloscope. The first pulse does not pass the SPR device and is irrelevant, the second pulse passes the SPR twice and the third pulse pass four times, etc. The period of the periodic pulses is determined by one round-trip time around the fiber loop. The length of the delay line is not important (about 30 meters in this case) as long as it guarantee that the recirculating pulses are well separated in time.

Pulse generator 2 is gated and synchronized by pulse generator 1 to produce a synchronized pulse train with a longer pulse width T as shown. This gated pulse applied on the RF port of the electroptic modulator is used for controlling its transmittance. During the time interval T when the gated pulse is applied on the electrooptic modulator, its transmittance is high and the fiber loop is closed, otherwise the loop is opened preventing the pulse to pass. This leads to the periodic opening of the EOM, which prevents the fiber loop from becoming a ring laser as the optical amplifier has gain. Here, the EOM acts as a loss-modulating optical switch with the switch closed (low loss) when the gated electrical pulse is applied to the RF port of the EOM, otherwise the switch is opened (high loss). The generation of the optical pulse train is summarized in Fig. 4.2.

An important issue relates to the detrimental affect of interference fringe on the sensitivity of the multipass SPR. If the fringe spacing (or the spot size) is smaller than the propagation decay length of the surface plasmon, one can expect a substantial decrease in SPR sensitivity in contrast with the case without interference effects. We have experienced just such an effect. The propagation decay length of the plasmon wave along the metal surface is given by $1/(2\mathrm{Im}(k_{sp}))$, where $k_0 = 2\pi/\lambda$, and ε_m and ε_s are

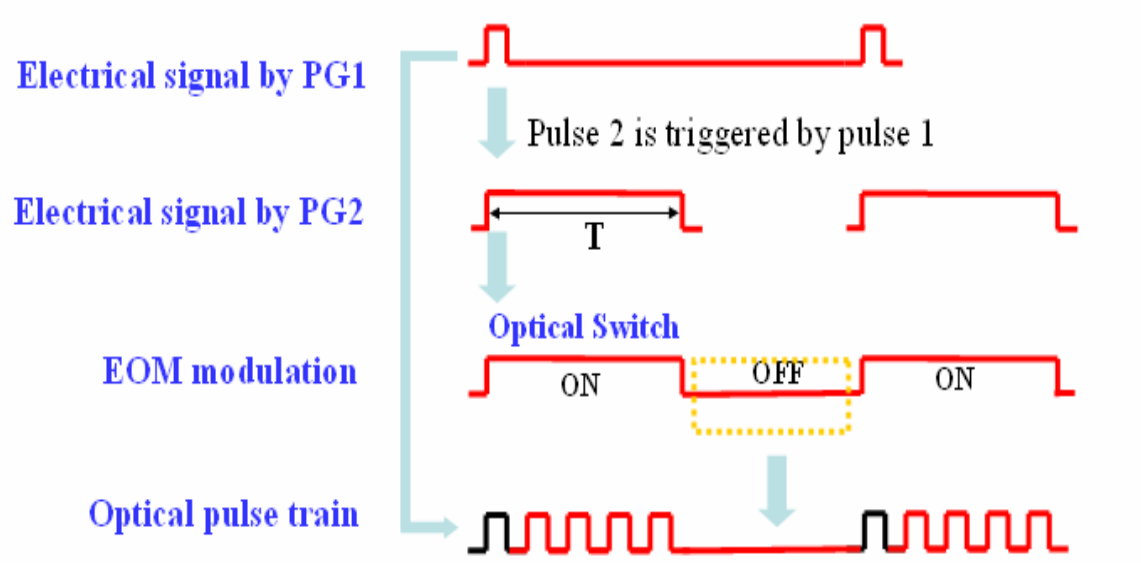

Fig. 4.2 The generation of the optical pulse train.

the gold and analyte dielectric constant respectively. Using $\varepsilon_m = (0.2+i.10.2)^2$ for gold and $\varepsilon_s = 1.3159^2$ for water, the propagation decay length is about 250 μm for a wavelength, λ, of 1.53 μm used in this experiment. Therefore, in this work, a corner cube replaces a mirror reflector that was used in reference 19. In addition, two collimators side-by-side are used for delivering and receiving light that passes the SPR surface instead of one collimator. The corner cube retro-reflect the light from one collimator back into the other collimator. With this method the light spot at the SPR surface does not overlap, avoiding the possible interference effects that occurs with the use of one collimator and a mirror reflector scheme. However, if the light source has low coherence

then the one collimator and one reflecting mirror scheme may still be used if the optical path length spacing between the mirror and the light spot at the SPR surface is longer than the coherence length of the light source.

To apply an electric field to the analyte solution, another Au-coated glass wafer is used as the top electrode. This field-assist process is the same as that shown in chapter III. The difference is that a positive voltage is applied to the top electrode so that positive ions are collected onto the bottom SPR surface. In this study, a light source wavelength of 1.53 μm compatible with erbium-doped fiber amplifier technology is used.

4.2 Experiment Results

First, the one pass SPR reflectivity profiles versus incident angle is measured for DI water as reference solution as explained in chapter III (see Fig. 3.2(b)). The presence of a substance with larger refractive index than the water's index shifts the resonance angle towards larger values. Thus, by setting the bias angle below the resonance angle, the reflected optical power increases with the solution's index.

To investigate and calibrate the 44-pass response with respect to changes of refractive index, various concentrations of salt solutions in DI water are prepared and measured in Fig. 4.3. The corresponding pulse signal amplitude of the 22th pulse associated with the various salt concentrations are measured and the result plotted in Fig. 4.4. Since each pulse corresponds to two passes and the total number of pulses is 22, the total number of passes is 44. Fig. 4.3 shows that the differential change in amplitude increases with the number of passes and salt concentration. The solution's index increas-

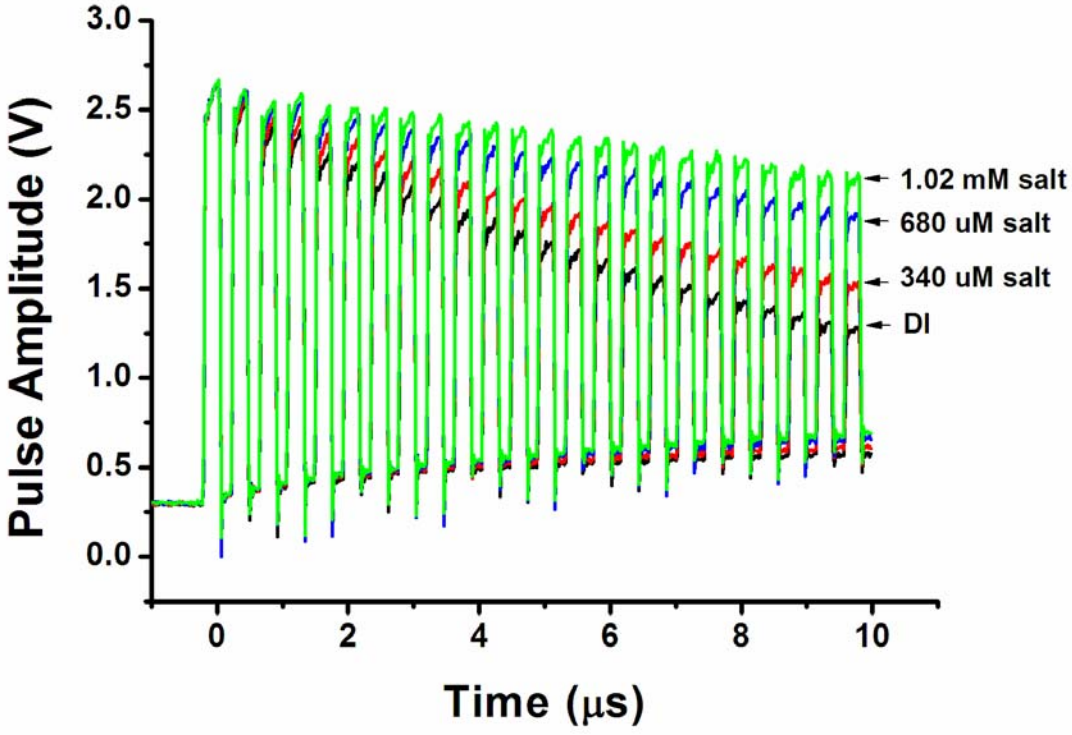

Fig. 4.3 Pulse amplitude versus number of passes for DI water, 340 μM salt, 680 μM and 1.02mM salt.

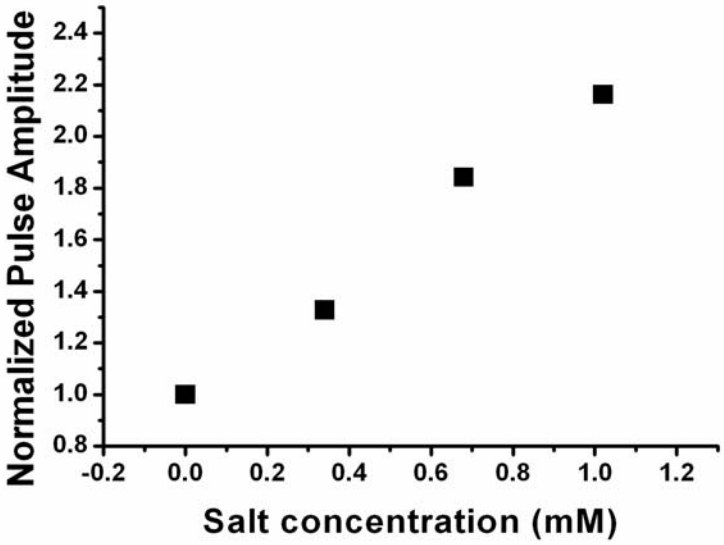

(a)

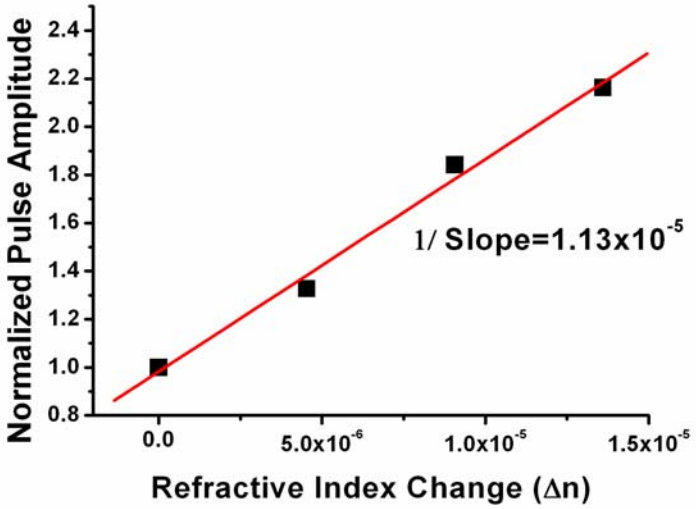

(b)

Fig. 4.4 (a) Normalized pulse amplitude for 44 passes versus salt concentration. (b) Normalized pulse amplitude for 44 passes versus refractive index change corresponding to the salt concentration.

es with the increase of salt concentration, which causes the reflected optical power to increase. Since the index can be calculated in terms of the salt concentration, we can calibrate the 44-pass response with respect to index change using salt solution. Fig. 4.3 shows that there is a gradual increase in the baseline signal with time, which is due to amplified spontaneous emission associated with the erbium-doped fiber amplifier itself. If the EOM gate is left closed for too long, the setup eventually becomes a ring laser, destroying the SPR function. Thus, the ultimate number of passes is limited by lasing effects.

From Fig. 4.3, the normalized 44-pass pulse signal with respect to salt concentration and its corresponding index's change are plotted in Fig. 4.4. As shown in Fig. 4.4(a), the normalized pulse signal increase is linearly proportional to salt concentration. The normalized pulse amplitude corresponding to the index change is shown in Fig. 4.4(b). The conversion from salt concentration to refractive index change, Δn, is by the formula: $n_w + \Delta n = n_s x + (1-x)n_w$,[59] where n_s and n_w are the refractive index of salt and water respectively, and x is the salt weight fraction. The refractive index change per the normalized pulse amplitude change, 1.13×10^{-5} gives the best fit to the measured data in Fig. 4.4(b). This allows us to predict the unknown index of a solution.

In chapter III, we studied a time-dependent SPR signal response for the attraction of negatively charged ions to the SPR surface. It has been demonstrated that the attraction of the negatively charged ions to the SPR surface lead to an increase in the SPR signal if the bias angle is below the resonance angle as indicated in Fig. 3.2(b). The

SPR signal increase due to the applied field indicates an increase of the refractive index due to the negative ions. In this study, a time-dependent SPR signal response due to the attraction of cations (positive ions) to the SPR surface is investigated. First, the SPR signal response to a 0.8V step voltage for DI water is measured as shown in Fig. 4.5 for both 2 passes and 44 passes. The 2-pass data is taken from the amplitude change of the second pulse from among the 22 pulses (note that the first do not pass through the SPR so is not considered). The 44 pass data is taken from the 22 pulse. The decrease in signal is presumably due to the attraction of the SPR surfaces of H^+ ions, which at a pH of 7 has a concentration of 10^{-7} M. The signal suddenly increase at about 220 second because the voltage is sudden switched to the opposite polarity to attract the negative OH^- ions to the SPR surface. Here, the SPR signal decrease means that the refractive index of the solution is locally reduced in the detection region. These observations are plausible because it is well known that the magnitude of the refractive index of materials in the optical regime is nominated by the electron response.

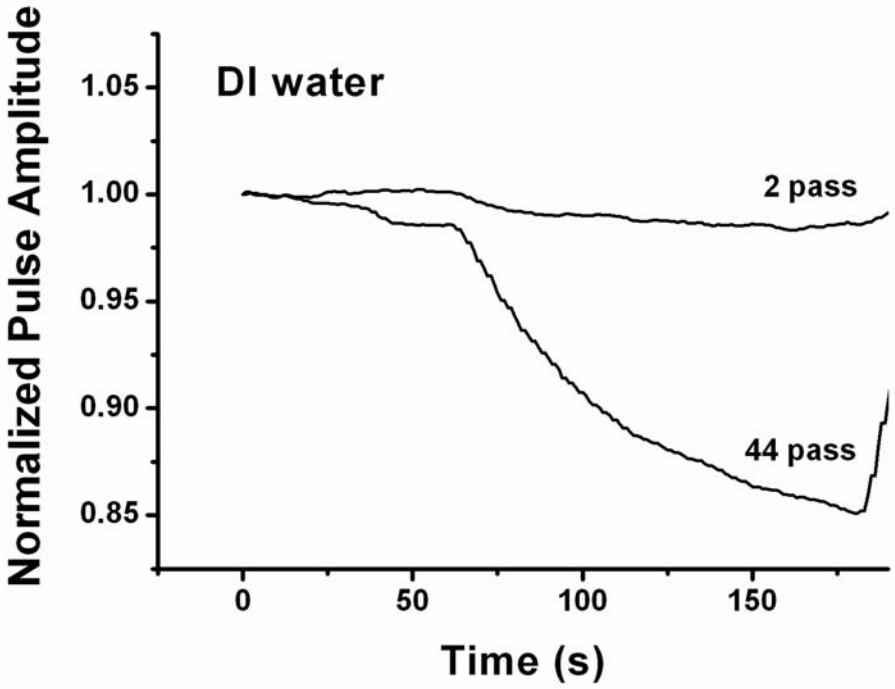

Fig. 4.5 Time-dependent SPR signals for DI water. (a) 2-pass (second pulse) (b) 44-pass (22th pulse). The applied voltage is 0.8V.

Thus, the detection of negative ions increases the refractive index while the detection of positive ions decreases the refractive index. It should be noted that SPR signal change induced by the applied voltage is a function of the refractive index change, and is a function of the concentration of cations (positive ions) in aqueous solution. Therefore, the refractive index of a concentration of cations in aqueous solution can be measured because the refractive index change per the fractional signal change can be predicted from Fig. 4.4(b). Moreover, 44 passes offer much better sensitivity than 2

passes, demonstrating that our device has good sensitivity to measure the index's change by the attraction of cations.

1M KOH and 1M NaOH are used as test solutions for measuring the refractive index of cations in aqueous solution. These solutions are chosen because K^+ and Na^+ ions are important to biological processes. A time-dependent 44-pass SPR signal response for the solution are measured and compared to DI water. For comparison, the one-pass reflectivity versus the incident angle is verified for the KOH and NaOH solutions respectively, then the bias point is set to the same level as that of DI water. Since KOH and NaOH is a strong base in aqueous solution and their degree of electrolytic dissociation are almost equal, we assume that 1M of K^+ and Na^+ ions exist in each aqueous solution. As predicted, Fig. 4.6 indicates that the SPR signal is decreased for both KOH and NaOH upon applying a positive voltage to the top electrode. This is due to the attraction to the SPR surface of K^+ and Na^+ ions. The degree of signal drop in response to the external field is proportional to the refractive index drop of cations in aqueous solution. Fig. 4.6 shows that the refractive index decrease by the attraction of

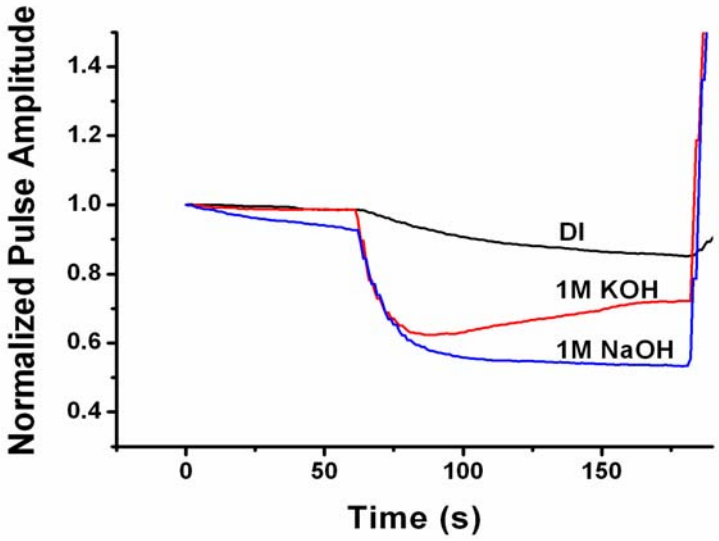

(a)

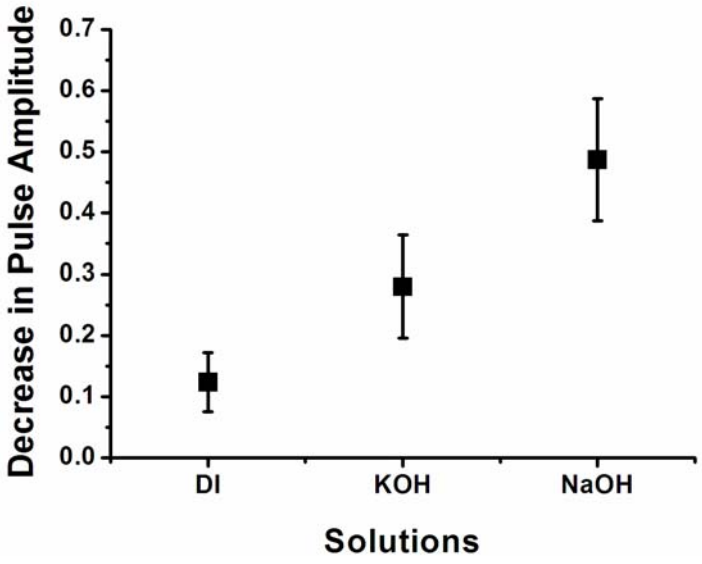

(b)

Fig. 4.6 (a) Time-dependence of the amplitude of the 22th pulse (44 pass) for DI water, 1M KOH and 1M NaOH. The applied voltage is 0.8V. (b) Fractional change in pulse amplitude obtained from (a).

Na^+ in aqueous solution to the SPR surface is greater than that of K^+. Moreover, according to Fig. 4.4 (b), we can calculate the refractive index change, Δn by the attraction of cations to the surface. In Fig. 4.6, the fractional change in pulse amplitude are about 0.15, 0.27 and 0.45 for DI water, 1M KOH solution and 1M NaOH solution, respectively. These values may vary by as much as 30 %, if the experiment is repeated by recycling the applied voltage. The variation is probably due to residual ions or molecules sticking to the SPR surface so that each run is not exactly the same. But the downward signal trend shown in Fig. 4.6 is always the same. We choose to apply a voltage of 0.8 volt so that it is below the water electrolysis voltage of 1.23 volt. Also a lower voltage protects the integrity of the gold surface for further use. If a higher voltage is applied, the signal magnitude will be bigger. Using the result of Fig. 4.4 (b), the calculated refractive index decrease are about 1.6×10^{-6}, 3.1×10^{-6} and 5.0×10^{-6} for DI water, 1M KOH solution and 1M NaOH solution, respectively. Additionally, the pulse signals for the solutions increase dramatically once the reversed voltage is applied This is due to the attraction of OH^- ions to the SPR surface. Especially, for the case of KOH and NaOH solutions, the stronger increase in the signal compared with DI water is shown. This is due to the attraction of much higher concentration of OH^- ions than that of DI water.

Additionally, a joule heating in solutions due to the applied field is investigated. A temperature increase in solution generally causes refractive index of the solution to decrease, thereby, we need to investigate if the decrease in the pulse amplitude shown in Fig. 4.5 and 4.6 are influenced by the joule heating due to the applied field. So, to

investigate the temperature increase due to the applied field, firstly, the current across the solution well filled with DI water was measured as shown in Fig. 4.7 (a). The current measurement was performed by connecting a 20 kohm of resistor in series with the solution wells and measuring the current across the resistor. From Fig. 4.7, we can calculate the energy due to the joule heating using $E = V\int Idt$ where V is the applied step voltage, 0.8V. The calculated energy E is $6.1296\times10^{-5} J$ for 150 s. The specific heat capacity of DI water, $C_{sp,water}$ is 4.186 $Jg^{-1}K^{-1}$ and the amount of water was filled in the solution well was 0.24 g. Therefore, the energy needed to increase 1K of temperature in DI water is 1.00464 J. Hence, the increase in temperature due to the applied field is about 6.1×10^{-5} ˚C for 150 s. This results in the change in refractive index of about -6×10^{-9}, which is not very significant with the local index change of -1.6×10^{-6} at the SPR surface due to the attraction of ions. In the same way, the refractive index change in 1M NaOH solution due to the joule heating was calculated from Fig. 4.7 (b) and it wad about -2.0×10^{-7} much less than the local index change of -5.0×10^{-6} due to the attraction of Na^{+} ions to the SPR surface (Specific heat capacity, $C_{sp,1M\ NaOH}$ is 3.975 $Jg^{-1}K^{-1}$).

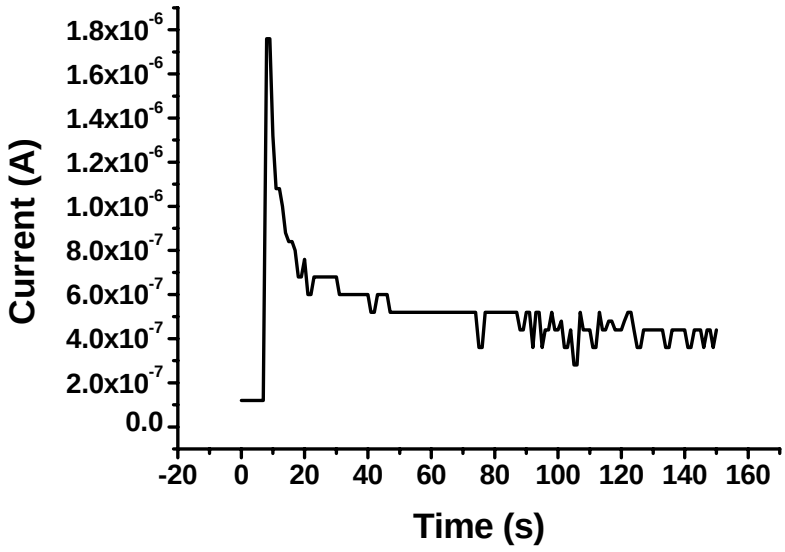

(a)

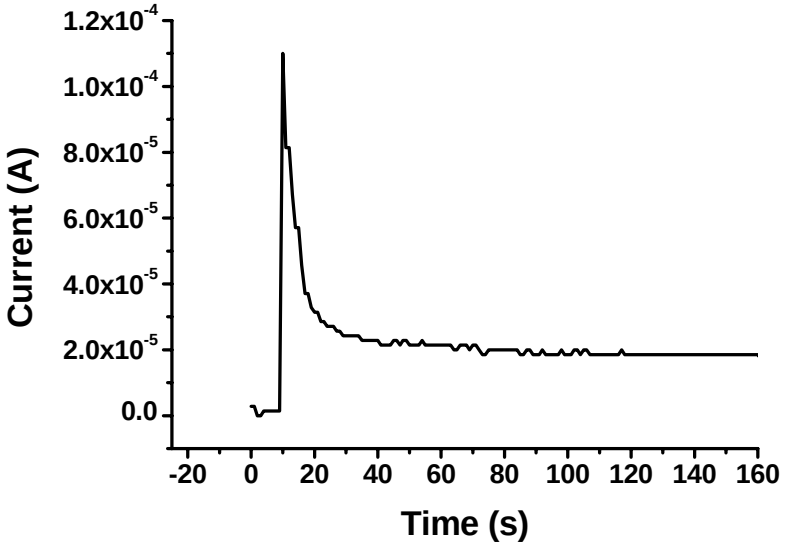

(b)

Fig. 4.7 Current flowing in (a) DI water and (B) 1M NaOH upon the turn-on of the step voltage of 0.8 V.

4.3 Summary

A field-assist 44-pass SPR fiber-optic technique for measurement of positive ions is demonstrated. Detection of positive ions gives a SPR signal that indicates a decrease in the refractive index, while the detection of negative ions gives a signal that indicates an increase in the refractive index. The detection of positive ions by the SPR technique may be a new method for studying ion exchange in cells. This study is ongoing, and will be a subject for future publications The multipass SPR sensor system offers sensitivity enhancement by a factor depending on the number of passes. This technique offers a method that can measure the refractive index with the improved sensitivity.

CHAPTER V

LIGHT TRANSMISSION THROUGH A METALLIC/DIELECTRIC NANO-OPTIC LENS

5.1 Principles for Lens Design

At this study, the wavelength of 405 nm is used because it is the shortest wavelength in the visible range. In the subwavelength metallic/dielectric structure, the surface plasmon excited at the interface of metal and dielectric plays an important role to enhance the transmission. Therefore, the SP wavevectors for various metals/dielectric are investigated in Fig. 5.1 from the dispersion relation below.

$$k_{sp,x} = \frac{\omega}{c}\sqrt{\frac{\varepsilon_m \varepsilon_d}{\varepsilon_m + \varepsilon_d}} \tag{5.1a}$$

$$k_{sp,zd} = \frac{\omega}{c}\sqrt{\frac{\varepsilon_d^2}{\varepsilon_m + \varepsilon_d}} \tag{5.1b}$$

where $k_{sp,x}$ denotes SP wave vector along *x*-direction and $k_{sp,zd}$ denotes the SP wave vector along *z*-direction in dielectric. Basically, the larger value of the real part of the wave vector means that the shorter wavelength of SP can be created. And, the imaginary value is inversely proportional to the propagation or decay length along *x* or *z* direction. Fig. 5.1 indicates that Ag offers the largest $k_{sp,x}$, $k_{sp,zd}$ among the investigated metals, meaning that Ag is the best metal to create the shortest wavelength of SP waves. Although the propagation length of SP in Ag/dielectric is shorter than of Ti or Al due to

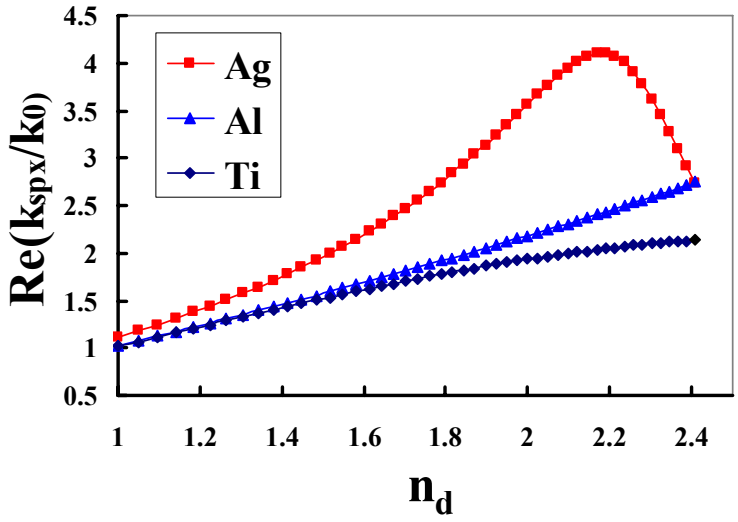

(a)

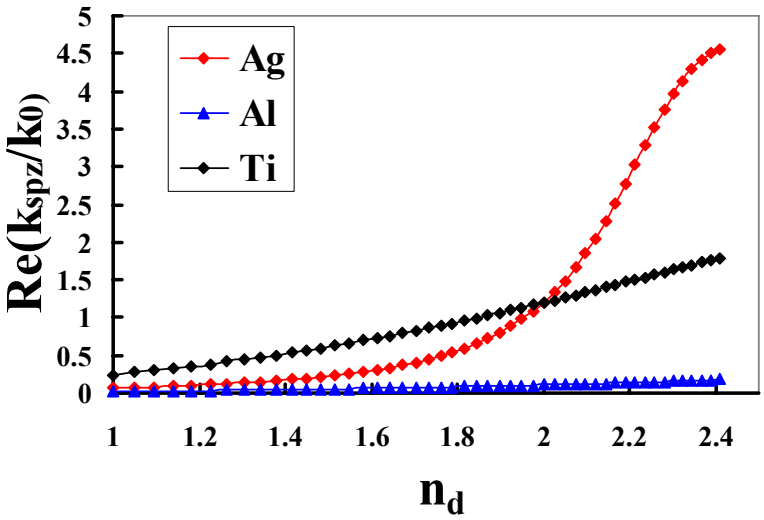

(b)

Fig. 5.1 Surface plasmon wavevector at the interface of metals and dielectric along (a) x-direction (b) z-direction.

larger imaginary values in Ag, the real part is presumably more prominent factor for the light focusing beyond the diffraction limit. Thus, we select Ag for our lens design.

In this study, the thickness of Ag thin film is fixed at 100 nm. In subwavelength structure, the thickness of metal is an important factor to influence the transmission efficiency. If the thickness is too thin, direct transmission through the thin metal film can be dominant due to the skip effect, causing the resolution of the focused beam to be degraded whereas too thick metal film cause the efficiency of light transmitted through subwavelength structure to be low. No direct transmission occurs at 100 nm of thickness as shown in Fig. 5.2 as well as 100 nm of thickness is not too thick to degrade the trans-

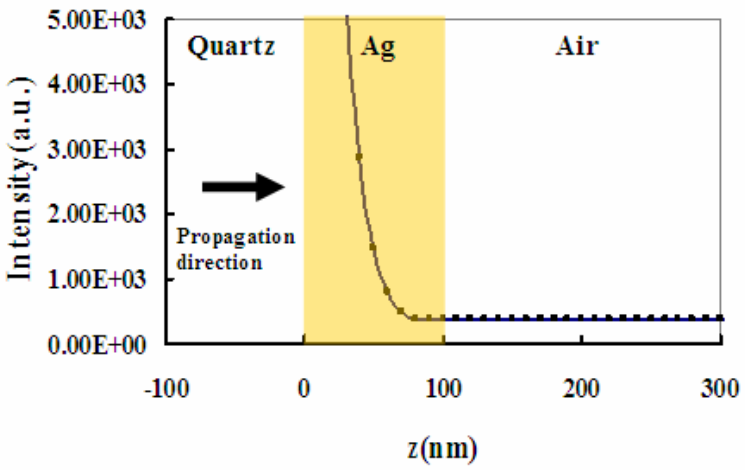

Fig. 5.2 Simulated intensity profile for the case that 405 nm wavelength of light is incident normally at the interface of quartz and Ag. The intensity of the incident light beam decays exponentially inside Ag, finally, there is no direct transmission across Ag film.

mission efficiency. Therefore, the thickness of Ag film is fixed at 100 nm at this study. In order to simply understand the role of the SP waves in nano-metallic slit, let us consider two closely placed parallel metallic plates. When TM polarized waves are incident through the metallic plates, the SP waves on the metallic slits will be coupled and propagate in the form of a waveguide mode. The propagation constant β can be calculated from the below equation.[31,61]

$$\tanh(\sqrt{\beta^2 - k_0^2\varepsilon_d}\, d/2) = \frac{-\varepsilon_d\sqrt{\beta^2 - k_0^2\varepsilon_m}}{\varepsilon_m\sqrt{\beta^2 - k_0^2\varepsilon_d}} \tag{5.2}$$

where k_0 is the wave vector of light in free space, ε_m and ε_d are the relative dielectric constant for the metal and the dielectric materials between slits. The imaginary part of β represents the decibel loss coefficient per unit length, however, it is ignorable for light propagation in short slits. Re(β/k_0) represents the effective refractive index (n_{eff}) in the slit and determines phase retardation and n_{eff} in the slit is dependent on the dielectric material in slit and the slit width, therefore, it can be calculated from Eq. (5.2) and shown in Fig. 5.3. Im(β/k_0) means the propagation loss in slit. Obviously, the dispersion relation in Fig. 5.3 offers a way of the modulation of n_{eff} in slit by varying the dielectric material in slit. When TM polarized incident wave is incident to the entrance of the metallic-dielectric slits, it excites the SPs, which propagate along slit surface up to the exit and finally, the SP waves radiate into light in free space[19]. Fig. 5.3 shows the propagation constant with respect to slit width for the different materials in slit. Generally, the real part of the propagation constant, Re(β/k_0) increases rapidly with the

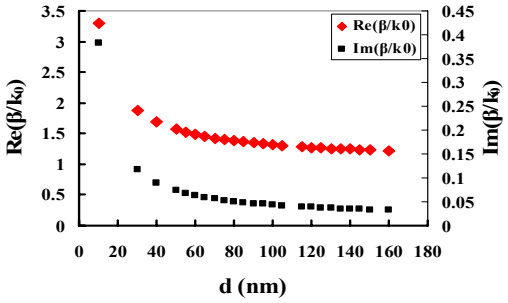

(a)

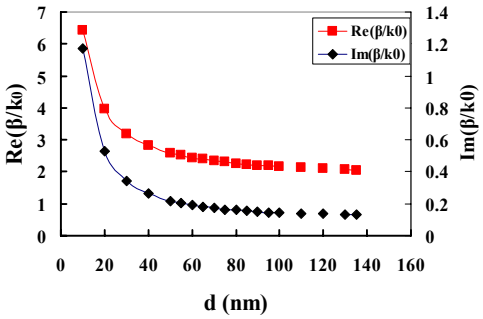

(b)

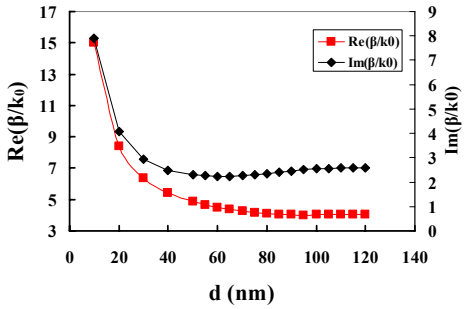

(c)

Fig. 5.3 Dependence of propagation constant of SPs in the slit on the slit width (d). The dielectric materials are (a) air (n_d=1), (b) PMMA (n_d=1.491) and (c) $LiNbO_3$ (n_d=2.2), respectively.

decreased slit width, indicating that the effective refractive index increases due to the highly SPs coupling, independently of the materials in slit. The propagation constant has the larger values as the refractive index in slit increases regardless of the slit width. The imaginary part of the propagation constant also increases with the decreased width. It is noted that the imaginary value is ignorable at low refractive index material in slit, however, it can not be ignorable as the refractive index increases. When the material in slit is $LiNbO_3$ (n_d=2.2), the SP propagation in slit is lossy even though the SPs coupling is maximized in slit. Therefore, both real and imaginary values of the propagation constant should be considered for the case that the high refractive index of material is used in the metallic slit.

Fig. 5.4 shows that the filling of dielectric material in slit with 150 nm of width generally allows the larger n_{eff}, and the refractive index of 2.2 in slit creates the maximum n_{eff}.

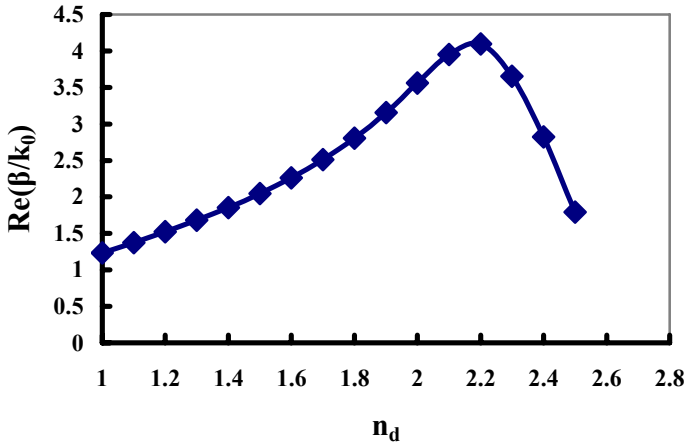

Fig. 5.4 Dependence of propagation constant of SPs in the slit on the refractive index of the slit (n_d)

In summary, at 405 nm of wavelength, Ag is the best metal for the excitation of SP and its thickness is fixed at 100 nm. And $LiNbO_3$ is selected as a dielectric material in Ag slit for this study.

5.2 FDTD Simulations and Results

5.2.1 Single Concentric Ring Structure

We designed the concentric ring structure in metal film since the propagating waves through a cylindrical symmetry converge or diverge in a free space. It consists of a quartz substrate coated with Ag thin film including subwavelength concentric ring aperture as shown in Fig.5.5. For three-dimensional simulation, a circularly polarized coherent plane wave, λ=405 nm is incident through the quartz substrate and the dielectric constant of Ag and quartz used at this wavelength are 5.1+1.0442i and 2.16, respectively.[62]

5.2.1.1 Effect of Dielectric Material in Slit

First of all, in order to investigate the filling effect of dielectric materials in slit on light transmission, we simulated the optical field exiting a simple lens with only one concentric ring. The Ag film thickness (t_m) is fixed at 100 nm and the circular ring radius (r) and ring slit width (d) are fixed at 3 um and 150 nm, respectively. Fig. 5.6 shows the optical field exiting a Ag/dielectric concentric ring structure for the cases that the concentric ring slit is filled with air, PMMA, Al_2O_3 and $LiNbO_3$, respectively. It indicates that the focusing and transmission through the lens is influenced by the

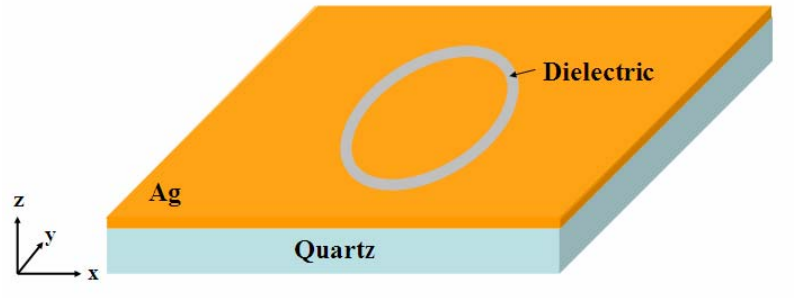

(a)

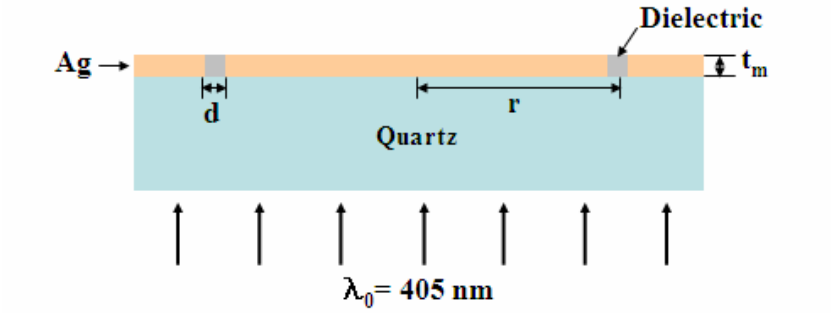

(b)

Fig.5.5 Schematics of the Ag/dielectric concentric ring structure. It is illuminated by a plane wave with 405 nm wavelength. (a) top view and right side (b) side view.

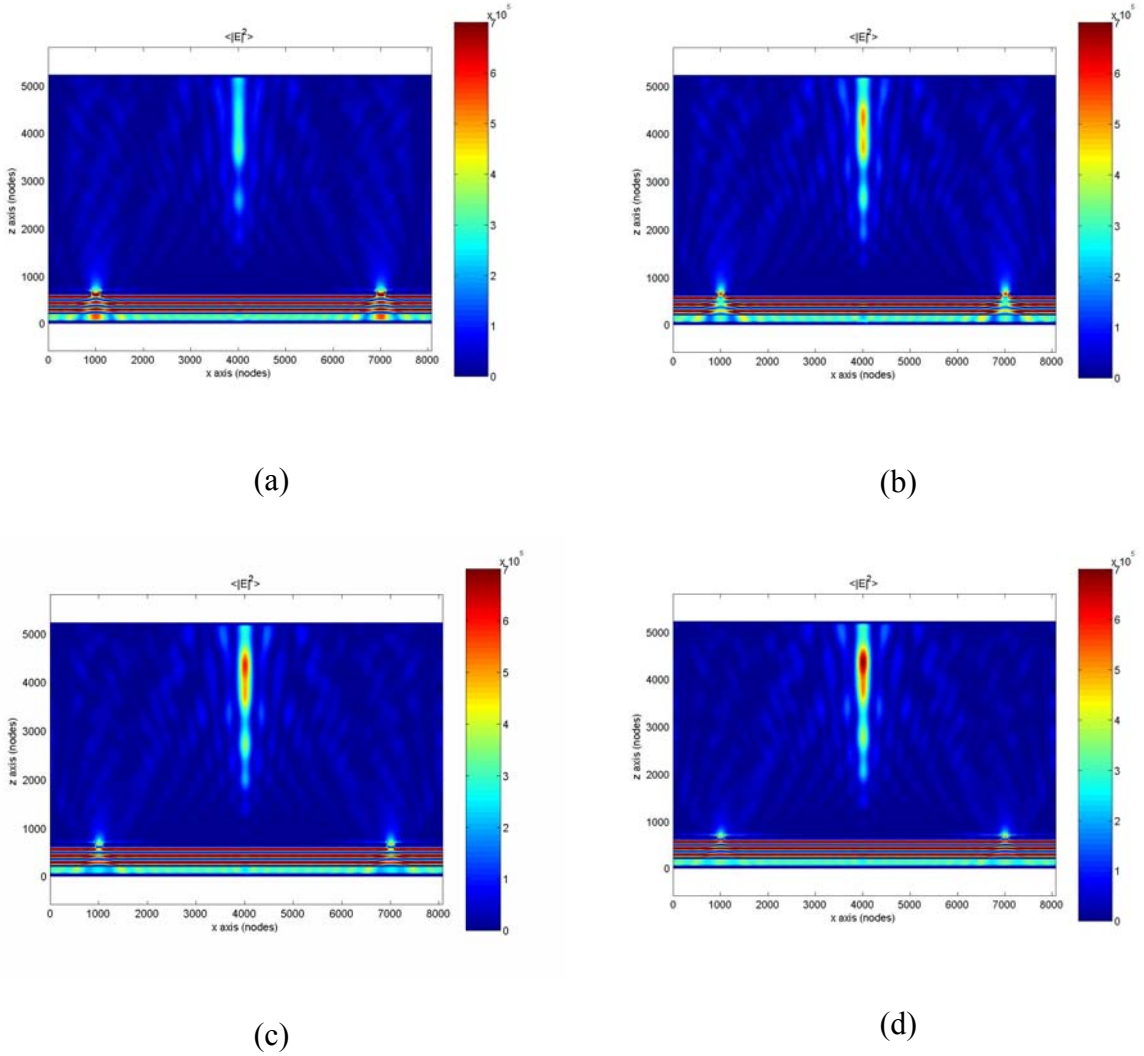

Fig. 5.6 The optical field exiting a lens at x-z plane, y=6um. The concentric ring slit is filled with (a) air (n_d=1.0), (b) PMMA (n_d=1.491), (c) Al_2O_3 (n_d=1.786) and (d) $LiNbO_3$ (n_d=2.2)

dielectric materials in slit. The intensity at the focal plane increases as the refractive index of material in slit increases.

In Fig. 5.7(a), the intensity of the beam versus *z* distance from the center point of the ring is compared as a function of refractive index in the concentric ring slit. It indicates that the focused beam intensity increases as the refractive index in the slit (n_d) increases. Additionally, the each focal points are shifted toward the longer focal length as n_d become larger. From 5.7(a) profiles with respect to $n_{d,}$ the transmission power is calculated by the summation of the focused light intensity along the focal axis and shown in Fig. 5.7(b). It demonstrates that the filling of the slit by a high refractive index medium can generally enhance the transmission efficiency, which shows the maximum at n_d=2.2. This result has good agreement with that of Fig. 5.4, therefore, it is evident that the increased coupling of SPs in a high refractive index enhances the transmission efficiency.

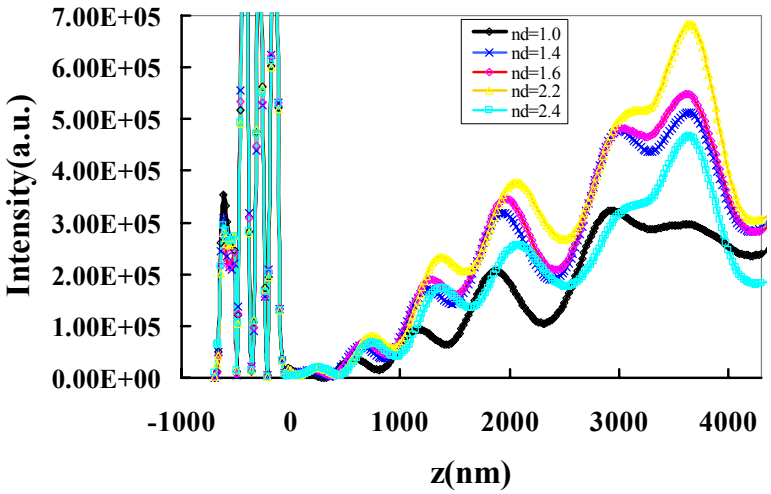

(a)

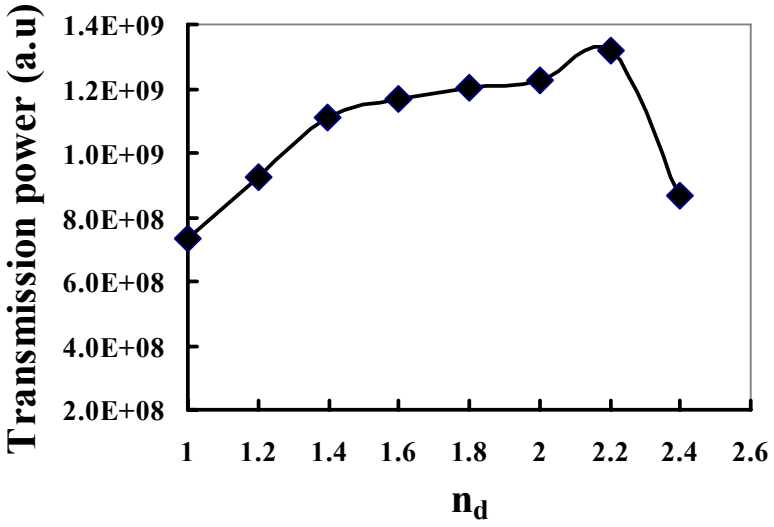

(b)

Fig. 5.7 (a) Intensity of the beam versus *z* distance from the center point of the ring for the refractive index in the concentric ring slit. (b) Light transmission power as a function of refractive index of the concentric ring slit.

5.2.1.2 Effect of Slit Width

In order to investigate the effect of slit width on light transmission through Ag/dielectric lens, the Ag film thickness (t_m) and the circular ring radius (r) are fixed at 100 nm and 3 μm, respectively. Since we verified that $LiNbO_3$ (n_d=2.2) is the dielectric material that produces the best transmission power in the previous section, the refractive index in the slit is fixed at 2.2. Fig. 5.8 shows the FWHM and intensity of the beam as a function of z distance from the center point of the ring. The FWHM representing the focused spot size is generally reduced as the slit width becomes smaller even though the lens with d=40 nm does not follow this tendency. It is because the effective refractive index in slit increases with the decreased slit width. However, the propagation loss at d=40 nm become quite prominent as shown in Fig. 5.3(c), presumably making the focusing resolution worse. The focused intensity along focal axis increases with the increase of slit width and the each focal points are shifted toward the longer focal length as slit width become larger.

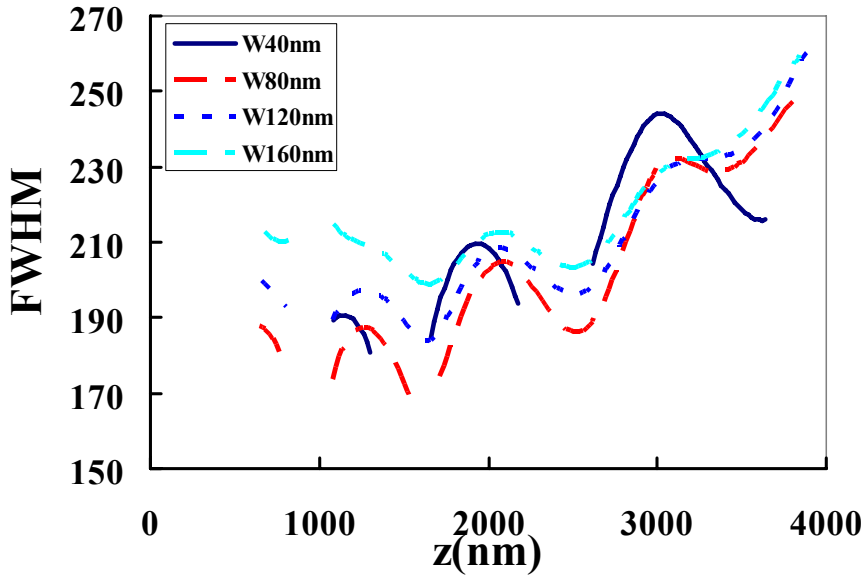

(a)

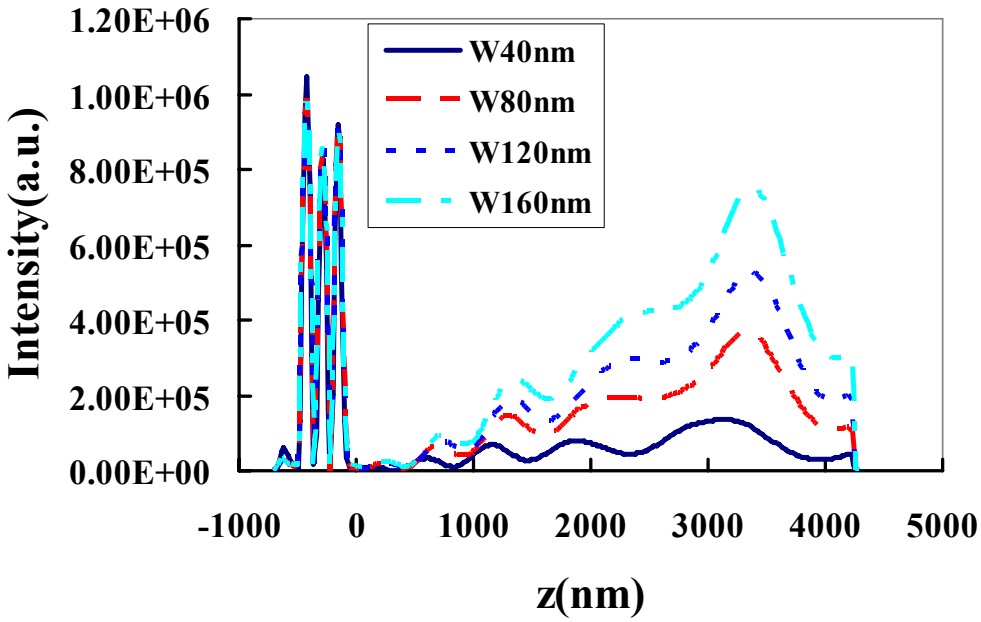

(b)

Fig.5.8 (a) FWHM and (b) Intensity of the beam versus z distance from the center point of the ring for the different slit width (d).

5.2.1.3 Effect of Concentric Ring Size

Fig. 5.9 shows the effect of ring size on beam focusing. It is seen that the FWHM of the beam size with respect to the propagation length from the exit plane increases gradually as the propagation length increases and the beam size generally decreases as the radius of ring become large. This means that this lens acts as the conventional optical lens under the designed conditions since the NA increases with the increase of lens size. Basically, the focusing characteristics is decided by interference between SP or evanescent waves and the propagating waves through aperture. At the lens with the concentric ring structure, more energy is coupled into the SP waves as the radius of ring is increased.[26] Therefore, Fig. 5.9 proves that the contribution of the enhancement of the SP or evanescent waves to the interference improves the resolution of the focused beam in the free space.

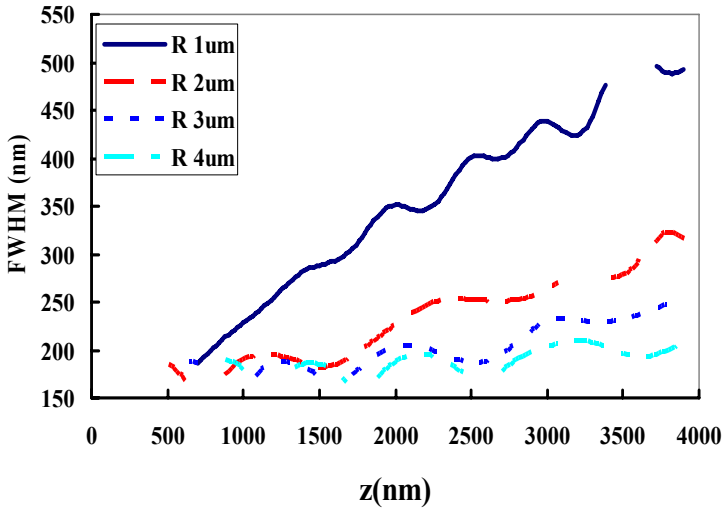

Fig. 5.9 FWHM versus z distance from the center point of the ring for the different radius of the concentric ring.

5.2.2 Multiple Concentric Ring Structure

Based on the numerical study on 1 ring structure, at this section, the multiple ring structure is investigated. For the multiple ring structure, basically, the interference of the SPs excited at the outer rings and those excited by the inner rings can enhance critically the intensity at the focal point by controlling the geometric parameter such as ring radius, grating pitch and slit width.[63] Moreover, this kinds of multiple ring structure can be tunable in wavelength, which might make it possible to be used for biosensor and color filter.

Since we found that $LiNbO_3$ (n_d=2.2) is the best dielectric material for the enhanced transmission efficiency in our design, a Ag/$LiNbO_3$ lens with three concentric ring structure was simulated and compared with a Ag/air structure in Figs. 5.10 and 11. Here, the slit width, d is fixed at 80 nm. Fig. 5.10 shows the optical field exiting a Ag/$LiNbO_3$ lens with three concentric ring. Here, the distance between an axial maximum and the exit surface of the lens is defined as its focal length. Also, the light-field distribution on the image plane can be defined as its point-spread function (PSF). Compared to Ag/air structure shown in Fig. 5.11, the Ag/$LiNbO_3$ lens shown in Fig. 5.10 indicates the critically improved lens effect. The Ag/$LiNbO_3$ lens creates the focal spot of 199 nm and depth of focus (DOF) of 1.4 um at the focal length of 1.88 um whereas the Ag-only lens makes the focal spot of 605 nm and the DOF of 0.9 um. Considering that the minimum of focused spot size depends on 0.61λ/NA corresponding to Rayleigh criterion, where NA is the numerical aperture, we found that Ag/ $LiNbO_3$ lens creates the focused beam beyond the diffraction limit at the extended focal length comparable to

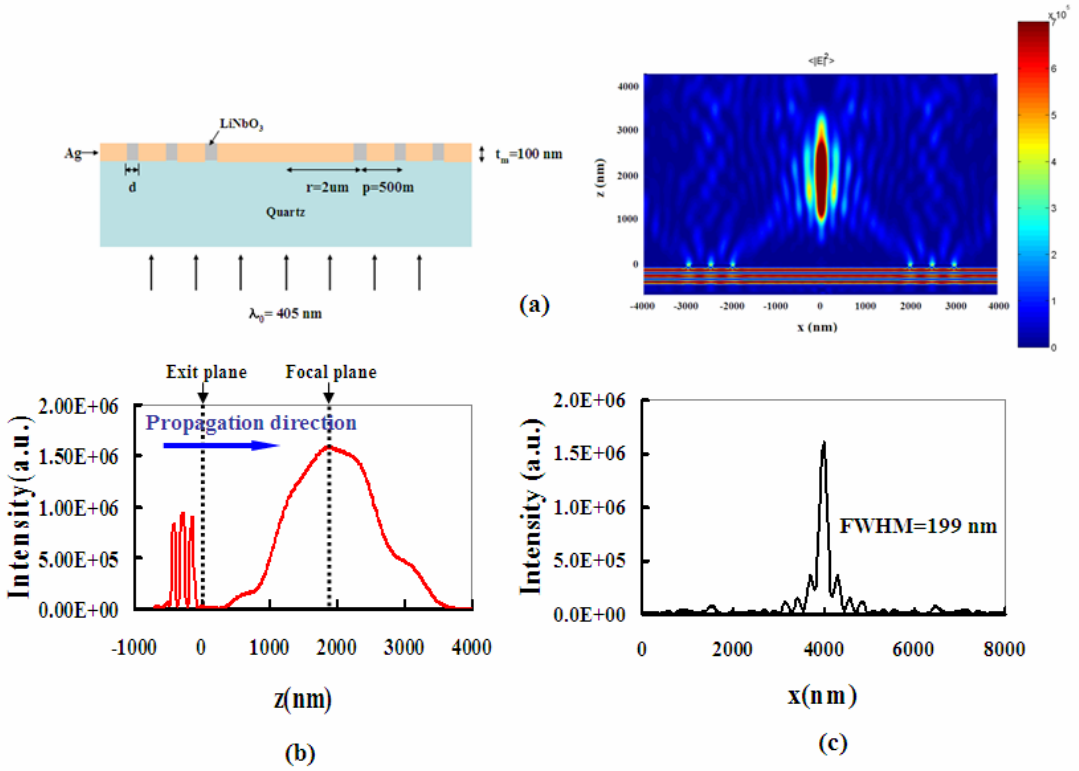

Fig. 5.10 Simulation of Ag/ $LiNbO_3$ lens. (a) (left side) Side view of the lens and (right side) the optical field exiting a lens at x-z plane, y=4μm, (b) Intensity of the beam as a function of z distance from the center point of the ring, (c) PSF (point spread function) at the focal point of 1.88 um.

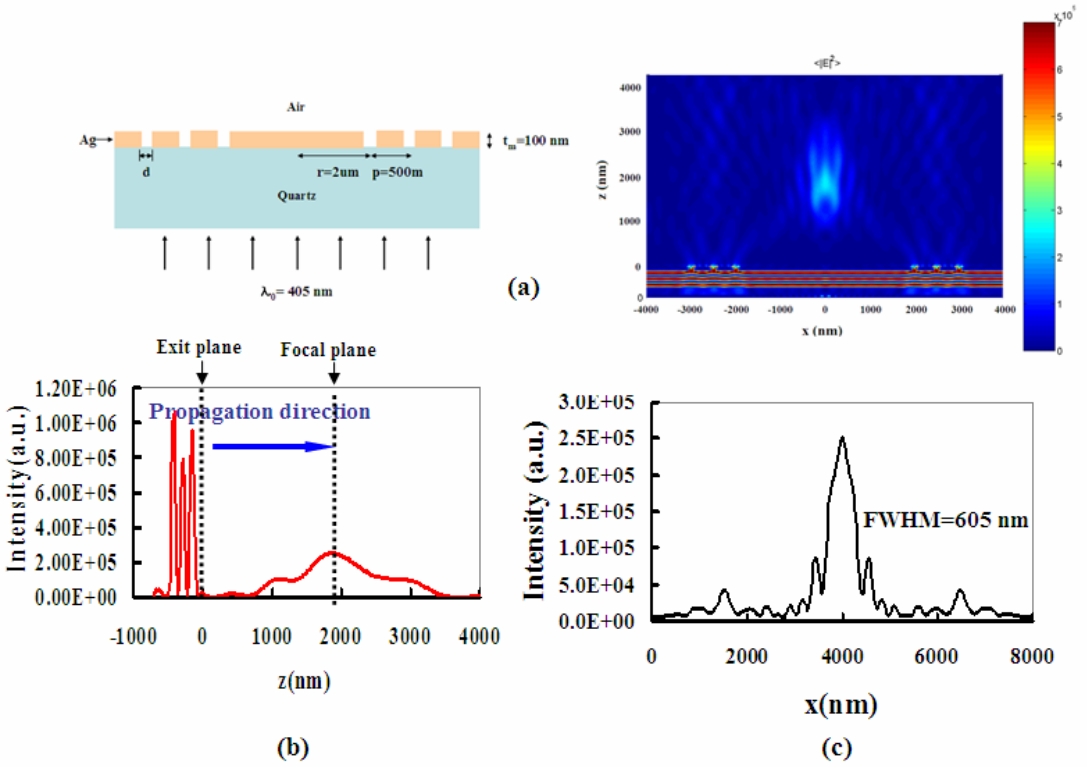

Fig. 5.11. Simulation of Ag-only lens. (a) (left side) Side view of the lens and (right side) the optical field exiting a lens at x-z plane, y=4μm, (b) Intensity of the beam as a function of z distance from the center point of the ring, (c) PSF (point spread function) at the focal point of 1.86 um.

7λ (Ideally, the spot size is 247 nm for NA=1). Its effective NA is 1.25. Also, the PSF at the focal planes in Ag/ $LiNbO_3$ indicates that the sidelobes diminish, which means that the contrast is improved on the image plane. Moreover, the transmission power is enhanced by 6 times than that of Ag/air lens. As mentioned above, this enhanced transmission efficiency and improved resolution are because n_{eff} become larger due to the excited SP waves in slits.

Additionally, near field and far-field focusing are investigated for the case that the dielectric layer are added to the slit. Fig. 5.12 shows the schematic of the structure and the focal intensity as a function of the dielectric thickness, t_d. The dielectric thickness varied from 0 to 400 nm. We observe that far field intensity at the focal plane is changed periodically in terms of the thickness, exhibiting a clear fabry-perot kind of behavior. The periodic behavior of the transmission has the period of $\lambda / \mathrm{Re}(\beta / k_0)$. It is believed that the dielectric layer can tune and enhance intensity at the focal point. Moreover, the near-field intensity can be enhanced and tuned by the dielectric layer similar to the far-field intensity even if the near field focal intensity has quasi-periodic function with respect to thickness, t_d. At a specific resonance condition, the near field intensity could be critically enhanced. Therefore, the dielectric layer offers a way of manipulating the transmitted light for both near-field and far-field focusing because it can modulate phase by the interference with the light transmitted through the adjacent concentric ring.

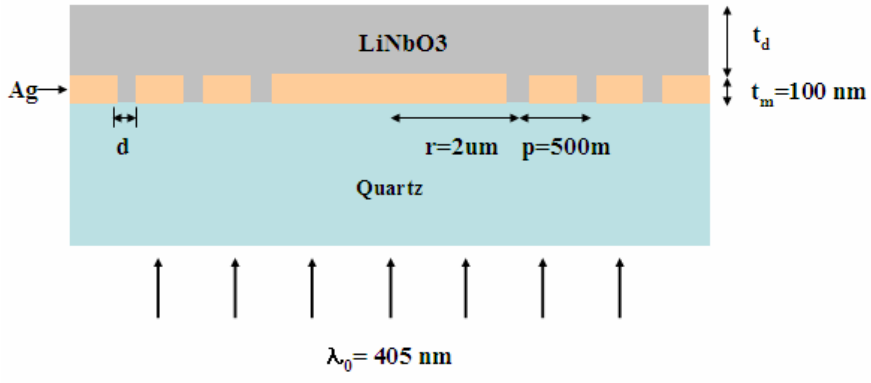

(a)

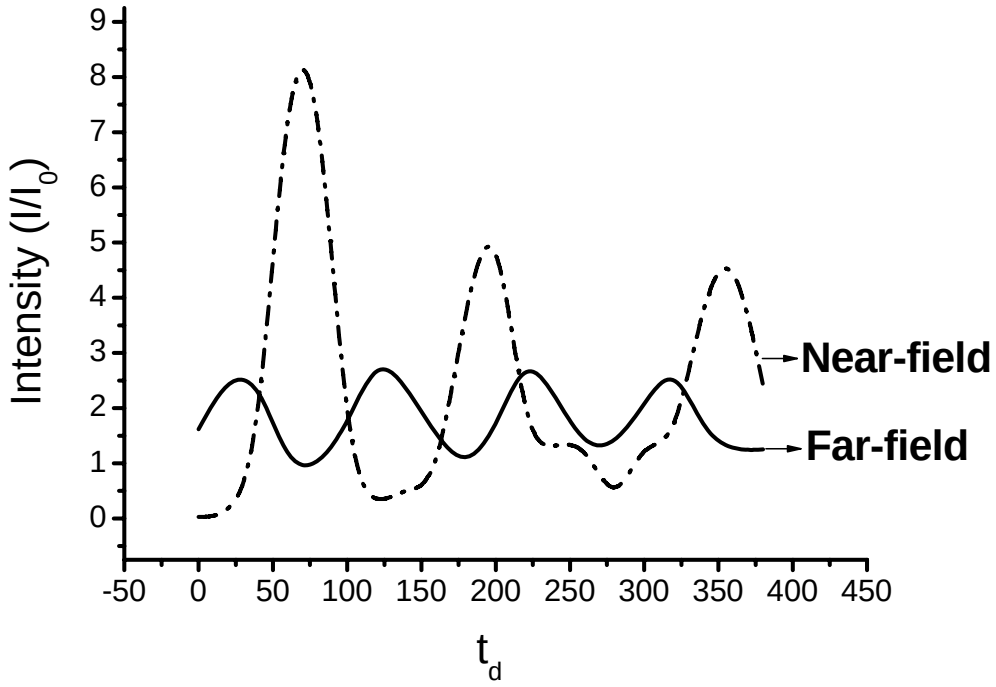

(b)

Fig. 5.12 Simulation of Ag/ $LiNbO_3$ layered lens. (a) Side view of the lens (b) Near-field and far-field focal intensity with respect to the dielectric thickness, t_d

Specifically, the optical field exiting a Ag/$LiNbO_3$ lens with t_d=120 nm is studied at Fig. 5.13. It indicates that when we compare the intensity for t_d =120 nm with that for t_d =0 nm (the dielectric is just filled in the slit), the intensity at the far-field focal plane is enhanced by a factor of 2. The intensity is enhanced by 12 times than that of Ag/Air structure described in Fig. 5.11.

Also, the controlled thickness of the dielectric layer can guide the transmitted waves at near-field region as shown in Fig. 5.14. Even if the purpose of study is focused on quasi-far field region, we found that the near field could be enhanced by the tuning of dielectric layer. The intensity at the near-field focal point is maximally enhanced by 255 times than the structure without the dielectric layer. The focal spot size is 90 nm which means that its NA is 2.8. For the sensitive sensing application, the enhancement of near-field intensity is a critical issue. Therefore, eventually the increased number of rings will enhance the near-field remarkably, thereby, this simple planar lens structure could be a good method for the sensing application.

In Ag/dielectric layered lens, the dielectric layer with high refractive index acts as a waveguide which allows more evanescent waves to be guided along the Ag/dielectric at the center of the ring.[22] Moreover, the diffracted light through the circular slits creates the evanescent wave not only at the interface of Ag/dielectric, but also at the interface of air/dielectric due to total internal reflection. It finally leads the critical enhancement of SP waves at specific dielectric thickness. Although this multi-ring structure is similar to the Fresnel zone plate (FZP), this metal-dielectric structure offer a simple way for the

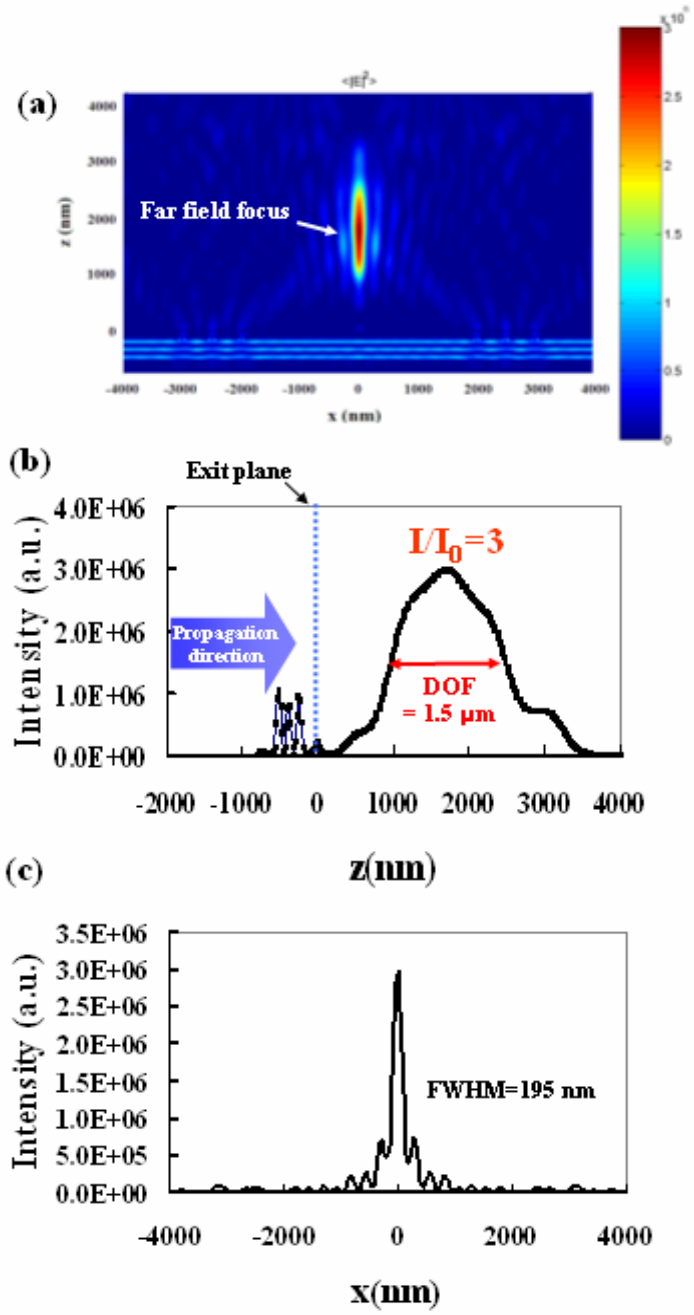

Fig. 5.13 Simulation of Ag/ $LiNbO_3$ layered lens with t_d=120 nm. (a) The optical field exiting a lens at x-z plane, y=4μm, (b) Intensity of the beam as a function of z distance from the center point of the ring (c) PSF (point spread function) at the focal point of 1.7 μm.

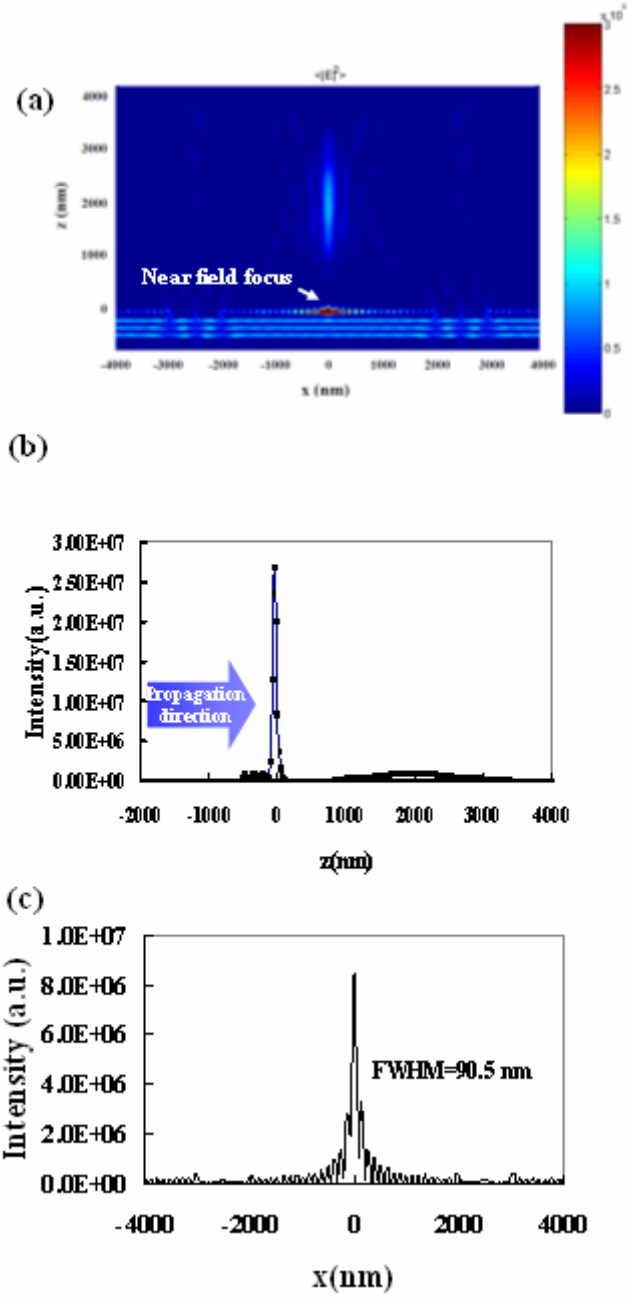

Fig. 5.14 Simulation of Ag/ $LiNbO_3$ layered lens with t_d=80 nm. (a) The optical field exiting a lens at x-z plane, y=4μm, (b) Intensity of the beam as a function of z distance from the center point of the ring (c) PSF (point spread function) at the exit plane.

real fabrication compared to the FZP because the outmost width requires the narrower slits for the improved resolution at FZP.

As follows, we can explain the reason why the Ag/dielectric lens generates the enhanced transmission and improved resolution at the extended focal length. Basically, at the concentric ring structure, the diffracted light gains a Δk along in-plane of the film which allows a portion of the incident light to excite a SP cylindrical waves, and finally, the energy is guided toward the center point of the ring. At cylindrical coordinate system (r, θ, z), the SP waves can be expressed as follows.[21]

$$\begin{aligned} H_{sp,\theta} &= \left(C_1 H_1^{(1)}\left(k_{sp,r} r\right) + C_2 H_1^{(2)}\left(k_{sp,r} r\right)\right)\exp\left(ik_{sp,z} z\right) \\ E_{sp,r} &= \frac{k_{sp,z}}{\omega\varepsilon} H_{sp,\theta} \\ E_{sp,z} &= \frac{i}{\omega\varepsilon}\left(\frac{H_{sp,\theta}}{r} + \frac{\partial H_{sp,\theta}}{\partial r}\right) \end{aligned} \tag{5.1}$$

where $H_{sp,\theta}$ is the θ component of the magnetic field and $E_{sp,r}$ and $E_{sp,z}$ are r and z components of the electric field, respectively. And $k_{sp,r}$ and $k_{sp,z}$ are the SP wave numbers in the r and z directions, respectively. $H_1^{(1)}$ and $H_1^{(2)}$ are the Hankel functions of the first and second kind, corresponding to outward and inward travelling cylindrical waves, respectively. C_1 and C_2 are the amplitudes of the corresponding waves. $k_{sp,r} = k_0\sqrt{\varepsilon_m \varepsilon_d / \left(\varepsilon_m + \varepsilon_d\right)}$ and $k_{sp,zd}$ in the dielectric is given by $k_{sp,zd} = k_0 \varepsilon_d / \sqrt{\varepsilon_m + \varepsilon_d}$, where k_0 is the wave number in free space and ε_m and ε_d are the permittivity of the metal and dielectric, respectively. Therefore, the excited SP waves are a complex function of $k_{sp,r}$ and $k_{sp,zd}$. For Ag/air at λ=405 nm, $k_{sp,r}$ =k_0(1.108+i0.026)

and $k_{sp,zd}$ =k_0(0.060-i0.4823), and for Ag/ $LiNbO_3$, $k_{sp,r}$ =k_0(4.093+i2.580) and $k_{sp,zd}$ =k_0(2.873-i3.676). The resulting focusing is formed by interference between the SP waves and the diffraction waves from slits, therefore, greater $k_{sp,r}$ and $k_{sp,zd}$ in Ag/dielectric interface may contribute to superfocusing if the excited SP waves can propagate to the extended length along z-direction.

5.3 Summary

The transmission of a normally incident plane wave through a Ag/dielectric layered concentric ring structure was studied. The focusing and transmission through the lens is influenced by the dielectric materials in slit. The intensity at the focal plane increases as the refractive index of material in slit increases. The FWHM representing the focused spot size generally is reduced as the slit width becomes smaller.

The Ag/ $LiNbO_3$ lens with the multiple ring structure creates the focal spot of 199 nm and the DOF of 1.4 um at the focal length comparable to 7λ. The effective NA of the focusing lens is 1.25. Moreover, the transmission power is enhanced by 6 times than that of Ag-only lens. With the addition of the dielectric layer, the far-field and near-field intensity at the focal plane is changed periodically in terms of the thickness, exhibiting a fabry-perot kind of behavior. It is clearly believed that the dielectric layer can remarkably tune and enhance intensity at the focal point.

CHAPTER VI

CONCLUSION

In my dissertation, “multi-pass fiber optic surface plasmon resonance sensor” and “nano-metallic surface plasmon lens” are presented.

The multi-pass SPR device is combined with field assist method to detect the charged ions or particles in a solution. The multipass feature increases the sensitivity by a factor equal to the number of passes. The field-assist feature forces charged particles/molecules to the SPR surface, increasing the concentration resolution. The attraction to the SPR surface of the negatively charged ions cause the increase in SPR signal while the attraction to the SPR surface of the positively charged ions cause the decrease in SPR signal.

At the field-assist 4-pass SPR device, NaCl solution and polystyrene latex beads were used as a test of this technique. For NaCl solution a detectable solute concentration of 2 μM equivalent to an index resolution of 2.6×10^{-8} is shown. 10 pM concentration of 47 nm diameter polystyrene beads can be detected, corresponding to an index resolution of 9×10^{-8}.

At the 44-pass SPR device, the 44 pass responses with respect to changes of refractive index of solution are calibrated by using various concentrations of salt solutions that offer known values of refractive index change. As a result, the refractive index of ions in a solution is predicted by measuring the degree of the SPR signal

response. Therefore, this technique offers a new method that can measure the refractive index of ions dissolved in a solution with the improved sensitivity.

For nano-metallic surface plasmon lens, the transmission of a normally incident plane wave through a Ag/dielectric layered concentric ring structure was studied. The dependency of transmission efficiency on the filling of dielectric materials in slits was investigated and we found that $LiNbO_3$ is a best dielectric material to enhance the transmission efficiency at 405 nm of wavelength. The Ag/ $LiNbO_3$ lens creates the focal spot of 196 nm and the DOF of 2 um at the focal length comparable to 7λ. The effective NA of the focusing lens is 1.26. Moreover, the transmission power is enhanced by 2.85 times than that of Ag-only lens. Therefore, our simple lens has the promising potential for the real application to the optical data storage and microscopy.

REFERENCES

[1] Y. Cui, Q. Q. Wei, H. K. Park and C. M. Lieber, Science **293,** 1289 (2001)

[2] J. Kameoka and H. G. Craighead, Sensors and Actuators B **77,** 632 (2001)

[3] B. Ilic B, Y. Yang and H. G. Craighead, Appl. Phys. Lett. **85,** 2604 (2004)

[4] B. Liedberg, I. Lundstrom and E. Stenberg, Sensors and Actuators B **11,** 63 (1993)

[5] X. Liu X, D. Song, Q. Zhang and Y. Tian, Trends in Analytical Chemistry **24,** 887 (2005)

[6] K. Matsubara, S. Kawata and S. Minami, Appl. Opt. **27,** 1160 (1988)

[7] J. Homola, S. S. Yee and G. Gauglitz, Sensors and Actuators B **54,** 3 (1999)

[8] W. L. Barnes, A. Dereux and T. W. Ebbesen, Nature **424,** 824 (2004)

[9] E. Kretschmann, Z. Phys. **241,** 313 (1971)

[10] A. Otto, Z. Phys. **216,** 398 (1968)

[11] I. Pockrand, J. D. Swalen, J. G. Gordon, M. R. Philpott, Surface Sci. **74,** 237 (1978)

[12] J. G. Gordon II, S. Ernst, Surface Sci. **101,** 499 (1980)

[13] C. Nylander, B. Liedberg, T. Lind, Sensor and Actuators **3,** 79 (1982)

[14] B. Liedberg, C. Nylander, I. Lundstrom, Sensors and Actuators **4,** 299 (1983)

[15] B. Liedberg, C. Nylander, I. Lundstrom, Biosensors Bioelectron. **10,** i (1995)

[16] K. Matsubara, S. Kawata, S. Minami, Appl. Opt. **27,** 1160 (1988)

[17] B. Liedberg, I. Lundstrom, E. Stenberg, Sensors and Actuators B **11,** 63 (1993)

[18] L. M. Zhang, D. Uttamchandani, Electron. Lett. **23,** 1469 (1988)

[19] C. B. Su and J. Kameoka, Meas. Sci. Technol. **19,** 015204 (2008)

[20] C. B. Su, J. Kameoka, B. Ilic, K. H. Chu and K. A. Chang, Appl. Phys. Lett. **89,** 071101 (2006)

[21] W. L. Barnes, A. Dereux and T. W. Ebbesen, Nature (London) **424**, 824 (2003).

[22] D. O. S. Melville and R. J. Blaikie, Opt. Exp. **13**, 2127 (2005)

[23] T. W. Ebbesen, H. J. Lezec, H. F. Ghaemi, T. Thio and P. A. Wolff, Nature **391**, 667 (1998)

[24] Z-B. Li, J-G. Tian, Z-B. Liu, W-Y. Zhou and C-P. Zhang, Opt. Exp. **13**, 29071 (2005)

[25] T. Thio, K. M. Pellerin, R. A. Linke, H. J. Lezec and T. W. Ebbesen, Opt. Lett. **26**, 1972 (2001)

[26] Z. Liu, J. M. Steele, W. Srituravanich, Y. Pikus, C. Sun and X. Zhang, Nano Lett. **5**, 1726 (2005)

[27] Z. Liu, N. Fang, T-J. Yen, and X. Zhang, Appl. Phys. Lett. **83**, 5184 (2003)

[28] E. X. Jin and X. Xu, Appl. Phys. Lett. **86**, 111106 (2005)

[29] C. Liu, N. Chen and C. Sheppard, Appl. Phys. Lett. **90**, 011501 (2007)

[30] Z. Sun and H. K. Kim, Appl. Phys. Lett. **85,** 642 (2004)

[31] R. Gordon and A. G. Brolo, Opt. Exp. **13,** 1933 (2005)

[32] P. Lalanne and J. P. Hugonin, Nature Physics **2,** 551 (2006)

[33] E. Ozbay, Science **311,** 189 (2006)

[34] C. Genet and T. W. Ebbesen, Nature **445,** 39 (2007)

[35] C. Huang and Y. Zhu, Active and Passive Electronic Components **2007**, 13

(2007)

[36] H. X. Yuan, B. X. Xu, B. Lukiyanchuk and T. C. Chong, Appl. Phys. A **89,** 397 (2007)

[37] N. Garcia and M. Nieto-Vesperinas, J. Opt. A: Pure Appl. Opt. **9,** 490 (2007)

[38] J. Weiner, Opt. Exp. **16**, 950 (2008)

[39] T. Xu, C. Du, C. Wang and X. Luo, Appl. Phys. Lett. **91,** 201501 (2007)

[40] W. Srituravanich, N. Fang, C. Sun, Q. Luo, and X. Zhang, Nano Lett. **4**, 1085 (2004)

[41] D. B. Shao and S. C. Chen, Nano lett. **6**, 2279 (2006)

[42] D. B. Shao and S. C. Chen, Opt. Exp. **13**, 6954 (2005)

[43] Z. Jacob, L. V. Alekseyev and E. Narimanov, Opt. Exp. **14**, 8247 (2006)

[44] T. D. Milster, F. Akhavan, M. Bailey, J. K. Erwin and D. M. Felix, Jpn. J. Appl. Phys. **40**, 1778 (2001)

[45] Z. Rao, J. A. Matteo, L. Hesselink, and J. S. Harris, Appl. Phys. Lett. **90**, 191110 (2007)

[46] X. Shi and L. Hesselink, Jpn. J. Appl. Phys. **41**, 1632 (2002)

[47] D. A. Fletcher, K. B. Crozier, C. F. Quate, G. S. Kino, K. E. Goodson, D. Simanovskii and D. V. Palanker, Appl. Phys. Lett. **77**, 2109 (2000)

[48] S. Seo, Nano scale devices for plasmonic nanolithography and rapid sensing of bacteria, Ph.D Dissertation, Texas A&M University, Department of Electrical Engineering, College Station, 2007.

[49] Y. Shin, Electro-optically tunable polarization independent add drop filter with relaxed bam splitters in $LiNbO_3$, Ph.D Dissertation, Texas A&M University, Department of Electrical Engineering, College Station, 2008.

[50] A. Yariv, *Quantum Electronics*, 3rd edition. (John Wiley & Sons, New York ,1989)

[51] A. Nichol, Grating coupled surface plasmon enhanced fluorescence spectroscopy, Ph.D Dissertation, Max Planck-Institute for Polymer Research, Mainz, Germany, 2005

[52] H. Raether, *Surface Plasmons on Smooth and Rough Surfaces and on Gratings*, (Springer-Verlag, New York, 1988)

[53] J. Conway, Efficient optical coupling to the nanoscale, Ph.D Dissertation, University of California Los Angeles, Department of Electrical Engineering, 2008.

[54] X. Shi, Resonant optical transmission through a single subwavelength aperture for near field applications, Ph.D dissertation, Stanford University (2003)

[55] C. Sonnichsen, Plasmons in metal nanostructures, Ph.D dissertation, University of Munich, Department of Physics, 2001

[56] K. Yee, IEEE Transactions on Antennas and Propagation, **14**, 802 (1966)

[57] K. J. Kataja, Numerical modeling of near field optical data storage, VTT electronics, 2005

[58] F. A. Glover and J. D. S. Goulden, Nature **200,** 1165 (1963)

[59] K. A. Chang, H. J. Lim and C. B. Su, Meas. Sci. Technol. **13,** 1962 (2002)

[60] M. S. Mohammadi, Journal of Dispersion Science and Technology **23,** 689 (2002)

[61] H. Shi, C. Wang, C. Du, X. Luo, X. Dong and H. Gao, Opt. Exp. **13**, 6815 (2005)

[62] M. J. Weber, *Handbook of Optical Materials*, (CRC Press, New York, 2003)

[63] J. M. Steele, Z. Liu, Y. Wang and X. Zhang, Opt. Exp. **14**, 5664 (2006)

APPENDIX A

WAVEVECTORS AND OPTICAL PROPERTY OF HIGHLY CONDUCTIVE MATERIALS

A.1. Silver (Ag) interfaced with air (n=1)

A.2. Aluminum (Al) interfaced with air (n=1)

A.3. Titanium (Ti) interfaced with air (n=1)

A.1. Silver (Ag) interfaced with air (n=1)

wavelength [nm]	n	k	ε = ε ' + i ε "		Ksp,x [ko]		Ksp,zd [ko]		Ksp,zm [ko]	
			ε '	ε "	Re	Im	Re	Im	Re	Im
827	0.27	5.79	-33.451	3.127	1.015	0.001	0.008	-0.175	0.266	5.878
620	0.27	4.18	-17.400	2.257	1.030	0.004	0.017	-0.245	0.261	4.304
496	0.24	3.09	-9.491	1.483	1.056	0.010	0.029	-0.339	0.224	3.264
413	0.23	2.27	-5.100	1.044	1.109	0.026	0.061	-0.482	0.195	2.523
381	0.23	1.86	-3.407	0.856	1.171	0.056	0.106	-0.617	0.165	2.192
354	0.21	1.42	-1.972	0.596	1.333	0.172	0.254	-0.901	0.036	1.929
344	0.23	1.13	-1.224	0.520	1.423	0.570	0.731	-1.110	0.317	-1.739
335	0.30	0.77	-0.503	0.462	0.681	0.737	1.130	-0.444	0.363	-0.745
329	0.53	0.40	0.121	0.424	0.542	0.272	0.899	-0.164	0.178	0.361
326	0.73	0.30	0.443	0.438	0.624	0.154	0.806	-0.120	0.409	0.300
318	1.30	0.36	1.560	0.936	0.813	0.077	0.596	-0.106	1.029	0.393
310	1.61	0.60	2.232	1.932	0.882	0.077	0.497	-0.137	1.374	0.654
302	1.73	0.85	2.270	2.941	0.915	0.083	0.445	-0.171	1.513	0.922
295	1.75	1.06	1.939	3.710	0.936	0.088	0.414	-0.200	1.545	1.147
288	1.73	1.13	1.716	3.910	0.943	0.092	0.406	-0.212	1.527	1.224
276	1.69	1.28	1.218	4.326	0.957	0.096	0.387	-0.237	1.494	1.386
261	1.61	1.34	0.797	4.315	0.964	0.103	0.385	-0.257	1.414	1.456
248	1.55	1.36	0.553	4.216	0.967	0.108	0.387	-0.270	1.352	1.482
225	1.45	1.34	0.307	3.886	0.968	0.119	0.401	-0.288	1.243	1.470
207	1.34	1.28	0.157	3.430	0.964	0.136	0.427	-0.307	1.119	1.416
191	1.25	1.18	0.170	2.950	0.953	0.154	0.464	-0.315	1.009	1.316
177	1.18	1.06	0.269	2.502	0.932	0.171	0.509	-0.312	0.918	1.189
165	1.14	0.91	0.472	2.075	0.897	0.179	0.557	-0.288	0.860	1.020
155	1.16	0.75	0.783	1.740	0.860	0.163	0.587	-0.239	0.875	0.834
138	1.33	0.56	1.455	1.490	0.845	0.107	0.568	-0.159	1.064	0.615
124	1.46	0.56	1.818	1.635	0.862	0.089	0.535	-0.144	1.208	0.613
113	1.52	0.56	1.997	1.702	0.869	0.083	0.521	-0.138	1.274	0.612
103	1.61	0.59	2.244	1.900	0.881	0.076	0.498	-0.135	1.374	0.643
95	1.66	0.64	2.346	2.125	0.890	0.076	0.482	-0.140	1.429	0.696
89	1.72	0.78	2.350	2.683	0.908	0.080	0.455	-0.160	1.499	0.846
86	1.64	0.88	1.915	2.886	0.914	0.094	0.457	-0.188	1.417	0.958
83	1.56	0.92	1.587	2.870	0.915	0.105	0.465	-0.207	1.331	1.006

A.2. Aluminum (Al) interfaced with air (n=1)

wavelength [nm]	n	k	ε = ε ' + i ε "		Ksp,x [ko]		Ksp,zd [ko]		Ksp,zm [ko]	
			ε '	ε "	Re	Im	Re	Im	Re	Im
827	2.75	8.31	-61.505	45.616	1.005	0.004	0.037	-0.109	2.727	8.364
775	2.63	8.60	-67.018	45.134	1.005	0.004	0.033	-0.107	2.608	8.651
729	2.14	8.57	-68.904	36.744	1.006	0.003	0.028	-0.110	2.129	8.628
689	1.74	8.21	-64.291	28.570	1.007	0.003	0.025	-0.117	1.728	8.264
653	1.49	7.82	-58.954	23.275	1.007	0.003	0.024	-0.124	1.476	7.883
620	1.30	7.48	-54.235	19.505	1.008	0.003	0.023	-0.131	1.292	7.545
564	1.02	6.85	-45.831	13.939	1.010	0.003	0.022	-0.144	1.007	6.919
517	0.83	6.28	-38.794	10.380	1.012	0.003	0.021	-0.158	0.815	6.363
477	0.70	5.80	-33.157	8.062	1.015	0.004	0.021	-0.172	0.684	5.887
443	0.60	5.39	-28.641	6.441	1.017	0.004	0.021	-0.187	0.587	5.479
413	0.52	5.02	-24.967	5.255	1.020	0.004	0.022	-0.201	0.512	5.125
387	0.46	4.71	-21.954	4.331	1.023	0.005	0.022	-0.215	0.449	4.817
365	0.41	4.43	-19.424	3.603	1.026	0.005	0.022	-0.230	0.396	4.542
344	0.36	4.17	-17.291	3.030	1.029	0.005	0.023	-0.245	0.351	4.298
326	0.33	3.95	-15.465	2.573	1.033	0.006	0.023	-0.260	0.314	4.078
310	0.29	3.74	-13.901	2.199	1.037	0.006	0.023	-0.275	0.282	3.880
295	0.27	3.55	-12.545	1.897	1.041	0.007	0.024	-0.291	0.254	3.701
282	0.24	3.38	-11.365	1.649	1.046	0.007	0.024	-0.308	0.231	3.537
270	0.22	3.22	-10.332	1.437	1.051	0.008	0.025	-0.325	0.210	3.388
258	0.21	3.08	-9.420	1.261	1.057	0.008	0.026	-0.342	0.191	3.252
155	0.07	1.66	-2.760	0.240	1.249	0.030	0.051	-0.749	0.039	2.078
146	0.06	1.53	-2.328	0.192	1.319	0.041	0.062	-0.861	0.021	2.016
138	0.06	1.40	-1.963	0.157	1.420	0.058	0.082	-1.009	0.002	-1.994
131	0.05	1.29	-1.651	0.126	1.577	0.091	0.117	-1.222	0.039	-2.033
124	0.04	1.18	-1.386	0.104	1.857	0.175	0.207	-1.569	0.124	-2.195
118	0.04	1.08	-1.156	0.086	2.491	0.543	0.590	-2.293	0.485	-2.702
113	0.04	0.98	-0.957	0.071	1.780	2.910	3.035	-1.707	2.784	-1.847
108	0.03	0.88	-0.779	0.058	0.305	1.821	2.073	-0.268	1.598	-0.330
103	0.03	0.79	-0.625	0.052	0.142	1.278	1.620	-0.112	1.006	-0.155
99	0.03	0.70	-0.489	0.048	0.093	0.974	1.394	-0.065	0.679	-0.098
95	0.04	0.61	-0.369	0.046	0.076	0.764	1.257	-0.046	0.462	-0.075
92	0.04	0.52	-0.266	0.042	0.065	0.601	1.166	-0.034	0.308	-0.058
89	0.05	0.42	-0.172	0.040	0.064	0.457	1.098	-0.027	0.187	-0.049
87	0.05	0.37	-0.136	0.040	0.066	0.400	1.075	-0.025	0.146	-0.046
86	0.06	0.33	-0.104	0.038	0.069	0.344	1.056	-0.022	0.109	-0.042
85	0.07	0.27	-0.070	0.037	0.075	0.282	1.036	-0.020	0.072	-0.039
84	0.09	0.21	-0.037	0.036	0.092	0.213	1.019	-0.019	0.037	-0.038
83	0.13	0.15	-0.008	0.038	0.128	0.151	1.003	-0.019	0.007	-0.039

A.3. Titanium (Ti) interfaced with air (n=1)

wavelength [nm]	n	k	ε = ε ' + i ε "		Ksp,x [ko]		Ksp,zd [ko]		Ksp,zm [ko]	
			ε '	ε "	Re	Im	Re	Im	Re	Im
827	2.98	3.32	-2.142	19.787	1.002	0.025	0.154	-0.163	2.902	3.401
775	2.74	3.30	-3.382	18.084	1.004	0.027	0.154	-0.176	2.662	3.387
729	2.54	3.23	-3.981	16.408	1.006	0.029	0.157	-0.188	2.460	3.323
689	2.36	3.11	-4.103	14.679	1.007	0.032	0.163	-0.201	2.277	3.209
653	2.22	2.99	-4.012	13.276	1.009	0.036	0.169	-0.212	2.133	3.095
620	2.11	2.88	-3.842	12.154	1.010	0.039	0.176	-0.222	2.020	2.990
590	2.01	2.77	-3.633	11.135	1.011	0.042	0.183	-0.232	1.915	2.885
564	1.92	2.67	-3.443	10.253	1.012	0.046	0.191	-0.242	1.821	2.790
539	1.86	2.56	-3.094	9.523	1.012	0.050	0.201	-0.250	1.756	2.683
517	1.81	2.47	-2.825	8.941	1.012	0.053	0.209	-0.256	1.701	2.596
496	1.78	2.39	-2.544	8.508	1.012	0.056	0.218	-0.261	1.667	2.518
477	1.75	2.34	-2.413	8.190	1.012	0.059	0.224	-0.265	1.634	2.470
459	1.71	2.29	-2.320	7.832	1.012	0.061	0.229	-0.271	1.591	2.423
443	1.68	2.25	-2.240	7.560	1.013	0.064	0.234	-0.275	1.558	2.385
428	1.63	2.21	-2.227	7.205	1.014	0.067	0.239	-0.283	1.505	2.349
413	1.59	2.17	-2.181	6.901	1.014	0.069	0.244	-0.289	1.462	2.312
400	1.55	2.15	-2.220	6.665	1.016	0.072	0.246	-0.295	1.421	2.295
387	1.50	2.12	-2.244	6.360	1.017	0.074	0.250	-0.303	1.368	2.269
376	1.44	2.09	-2.295	6.019	1.020	0.078	0.253	-0.314	1.306	2.244
365	1.37	2.06	-2.367	5.644	1.023	0.082	0.257	-0.326	1.234	2.220
354	1.30	2.01	-2.350	5.226	1.027	0.087	0.264	-0.340	1.159	2.177
344	1.24	1.96	-2.304	4.861	1.030	0.093	0.271	-0.354	1.094	2.134
335	1.17	1.90	-2.241	4.446	1.034	0.101	0.281	-0.371	1.018	2.082
326	1.11	1.83	-2.117	4.063	1.037	0.110	0.295	-0.388	0.949	2.020
322	1.08	1.78	-2.002	3.845	1.038	0.117	0.307	-0.397	0.912	1.974
318	1.06	1.73	-1.869	3.668	1.038	0.124	0.320	-0.404	0.885	1.927
310	1.04	1.62	-1.543	3.370	1.033	0.140	0.351	-0.412	0.847	1.818
295	1.06	1.45	-0.979	3.074	1.012	0.161	0.405	-0.402	0.839	1.637
282	1.13	1.33	-0.492	3.006	0.986	0.164	0.437	-0.370	0.896	1.497
270	1.17	1.29	-0.295	3.019	0.976	0.161	0.445	-0.353	0.934	1.447
258	1.21	1.23	-0.049	2.977	0.963	0.158	0.457	-0.334	0.971	1.376
248	1.24	1.21	0.074	3.001	0.958	0.154	0.458	-0.323	1.002	1.351
238	1.27	1.20	0.173	3.048	0.955	0.150	0.456	-0.313	1.034	1.336
230	1.17	1.16	0.023	2.714	0.952	0.169	0.483	-0.334	0.918	1.303
221	1.24	1.21	0.074	3.001	0.958	0.154	0.458	-0.323	1.002	1.351
214	1.21	1.22	-0.024	2.952	0.961	0.159	0.460	-0.332	0.970	1.365
207	1.15	1.21	-0.142	2.783	0.963	0.170	0.472	-0.348	0.902	1.361
200	1.11	1.18	-0.160	2.620	0.960	0.180	0.487	-0.355	0.853	1.333
194	1.08	1.14	-0.133	2.462	0.953	0.190	0.505	-0.358	0.814	1.291
188	1.04	1.06	-0.042	2.205	0.936	0.204	0.539	-0.354	0.757	1.204
182	1.05	1.02	0.062	2.142	0.925	0.203	0.550	-0.341	0.764	1.156
177	1.06	0.97	0.183	2.056	0.911	0.201	0.562	-0.325	0.771	1.096
172	1.07	0.95	0.242	2.033	0.906	0.198	0.565	-0.317	0.781	1.072
168	1.11	0.94	0.349	2.087	0.904	0.187	0.557	-0.303	0.827	1.057
163	1.09	0.92	0.342	2.006	0.898	0.192	0.568	-0.303	0.802	1.035
159	1.11	0.93	0.367	2.065	0.901	0.187	0.560	-0.301	0.826	1.045
155	1.10	0.94	0.326	2.068	0.903	0.190	0.560	-0.306	0.816	1.058
151	1.10	0.95	0.308	2.090	0.906	0.190	0.557	-0.309	0.816	1.070
148	1.08	0.95	0.264	2.052	0.906	0.195	0.562	-0.314	0.793	1.071

144	1.04	0.96	0.160	1.997	0.908	0.206	0.570	-0.328	0.747	1.086
141	1.02	0.95	0.138	1.938	0.905	0.212	0.579	-0.331	0.722	1.076
138	1.00	0.94	0.116	1.880	0.902	0.218	0.588	-0.335	0.697	1.066
135	0.97	0.93	0.076	1.804	0.899	0.227	0.600	-0.341	0.660	1.057
132	0.95	0.91	0.074	1.729	0.892	0.234	0.613	-0.341	0.634	1.034
129	0.94	0.90	0.074	1.692	0.888	0.237	0.619	-0.340	0.621	1.022
127	0.91	0.88	0.054	1.602	0.880	0.248	0.636	-0.343	0.583	1.000
124	0.89	0.88	0.018	1.566	0.880	0.255	0.643	-0.349	0.558	1.001
122	0.86	0.85	0.017	1.462	0.866	0.266	0.664	-0.347	0.519	0.965
119	0.85	0.83	0.034	1.411	0.857	0.269	0.674	-0.342	0.505	0.940
117	0.81	0.79	0.032	1.280	0.836	0.283	0.704	-0.337	0.453	0.890
115	0.80	0.76	0.062	1.216	0.821	0.284	0.717	-0.326	0.441	0.851
113	0.79	0.72	0.106	1.138	0.800	0.282	0.731	-0.309	0.429	0.799
111	0.81	0.69	0.180	1.118	0.791	0.268	0.729	-0.290	0.456	0.762
109	0.81	0.69	0.180	1.118	0.791	0.268	0.729	-0.290	0.456	0.762
107	0.79	0.68	0.162	1.074	0.782	0.274	0.740	-0.290	0.431	0.749
105	0.78	0.67	0.160	1.045	0.775	0.277	0.747	-0.287	0.419	0.735
103	0.77	0.65	0.170	1.001	0.764	0.276	0.756	-0.279	0.408	0.709
97	0.76	0.55	0.275	0.836	0.717	0.251	0.776	-0.232	0.407	0.585
94	0.76	0.52	0.307	0.790	0.705	0.240	0.779	-0.217	0.411	0.549
91	0.76	0.48	0.347	0.730	0.691	0.225	0.783	-0.198	0.417	0.503
89	0.77	0.45	0.390	0.693	0.684	0.210	0.781	-0.184	0.432	0.469
86	0.77	0.42	0.417	0.647	0.675	0.198	0.783	-0.170	0.436	0.436
84	0.79	0.38	0.480	0.600	0.671	0.175	0.777	-0.152	0.464	0.394

APPENDIX B

TEMPEST INPUT SOURCE CODE

Simulation Parameters;

- Material: Ti, Incident Wavelength: 405 nm, Node Size: 30nm
- $a = 150$ nm (ring width), $r = 3$ μm (ring radius), $t = 100$ nm (metal thickness)

```
wavelength 0.405
x_node 267
y_node 267
z_node 200
x_dim 8.0

plane_source xy position 0 8 0 8 0.2 1 0 0 1 0 uniform 0 0
plane_source xy position 0 8 0 8 0.2 0 1 0 1 90 uniform 0 0

rectangle position 0 8 0 8 0.0 6.0 index 1.0 0.0
rectangle position 0 8 0 8 0.1 0.4 index 1.47 0.0
rectangle position 0 8 0 8 0.4 0.5 dispersive 1.57 2.16

zcylinder position 3.07 0.4 0.5 4 4 index 1.0 0.0
zcylinder position 2.92 0.4 0.5 4 4 dispersive 1.57 2.16

rectangle position 0 8 0 8 0.0 0.1 pml 0 0 -1 2.16 1 0 0
rectangle position 0 8 0 8 5.9 6.0 pml 0 0 1 1.0 1 0 0

plot ex steady 0.00 position 0 8 4 4 0.1 5.9 exi
plot ey steady 0.00 position 0 8 4 4 0.1 5.9 eyi
plot ez steady 0.00 position 0 8 4 4 0.1 5.9 ezi

plot ex steady 0.25 position 0 8 4 4 0.1 5.9 exq
plot ey steady 0.25 position 0 8 4 4 0.1 5.9 eyq
plot ez steady 0.25 position 0 8 4 4 0.1 5.9 ezq

plot ex steady 0.00 position 0 8 0 8 0.52 0.52 gxi
plot ey steady 0.00 position 0 8 0 8 0.52 0.52 gyi
plot ez steady 0.00 position 0 8 0 8 0.52 0.52 gzi

plot ex steady 0.25 position 0 8 0 8 0.52 0.52 gxq
plot ey steady 0.25 position 0 8 0 8 0.52 0.52 gyq
plot ez steady 0.25 position 0 8 0 8 0.52 0.52 gzq

plot refractive position 0 8 4 4 0 6 ri1
plot refractive position 0 8 0 8 0.52 0.52 ri2
```

APPENDIX C

MATLAB SCRIPT FILES [54]

C.1. Plotam6.m

C.2. Plotbin.m

C.3. Fwhm.m

C.1. Plotam6.m

```
function [x,y,g] = plotam6(file,dx);
% comment
fp1=fopen([file 'xi']);
fp2=fopen([file 'xq']);
fp3=fopen([file 'yi']);
fp4=fopen([file 'yq']);
fp5=fopen([file 'zi']);
fp6=fopen([file 'zq']);
size1=fread(fp1,3,'int')
size2=fread(fp2,3,'int')
size3=fread(fp3,3,'int')
size4=fread(fp4,3,'int')
size5=fread(fp5,3,'int')
size6=fread(fp6,3,'int')

[ff,ms]=min(size1);

if ms==1
   nx=size1(2);
   ny=size1(3);
   xlab='y axis (nodes)';
   ylab='z axis (nodes)';
end

if ms==2
   nx=size2(1);
   ny=size2(3);
   xlab='x axis (nodes)';
   ylab='z axis (nodes)';
end

if ms==3
   nx=size1(1);
   ny=size1(2);
   xlab='x axis (nodes)';
   ylab='y axis (nodes)';
end

%nx=401; ny=401;
disp([nx ny])

a=fread(fp1,[nx ny],'single');
b=fread(fp2,[nx ny],'single');
c=fread(fp3,[nx ny],'single');
d=fread(fp4,[nx ny],'single');
e=fread(fp5,[nx ny],'single');
f=fread(fp6,[nx ny],'single');
size(a)

a=a(:,:,1);
b=b(:,:,1);
```

```
c=c(:,:,1);
d=d(:,:,1);
e=e(:,:,1);
f=f(:,:,1);
g=a.*a+b.*b+c.*c+d.*d+e.*e+f.*f;
g=0.5*g;
x=dx*(0:(nx-1)); y=dx*(0:(ny-1));
pcolor(x,y,g'); shading('flat'); caxis([0 2*mean(g(:))]); %colormap('hot');
axis equal
colorbar;
xlabel(xlab);
ylabel(ylab);
title('<|E|^2>');

fclose(fp1);
fclose(fp2);
fclose(fp3);
fclose(fp4);
fclose(fp5);
fclose(fp6);
```

C.2. Plotbin.m

```
function a=plotbin(file1)
% comment
fp1=fopen(file1);
size1=fread(fp1,3,'int')

if size1(1)==1
   nx=size1(2);
   ny=size1(3);
   xlab='y axis (nodes)';
   ylab='z axis (nodes)';
end

if size1(2)==1
   nx=size1(1);
   ny=size1(3);
   xlab='x axis (nodes)';
   ylab='z axis (nodes)';
end

if size1(3)==1
   nx=size1(1);
   ny=size1(2);
   xlab='x axis (nodes)';
   ylab='y axis (nodes)';
end

a=fread(fp1,[nx ny],'float');
if ny==1,
plot(a);
else
pcolor(a');
%axis('equal');
colormap('hot');
shading('flat');
colorbar;
xlabel(xlab);
ylabel(ylab);
end
title('Electric Field');
fclose(fp1);
```

C.3. Fwhm.m

```
function width = fwhm(x,y)

y = y / max(y);
N = length(y);
lev50 = 0.5;

if y(1) < lev50
	[garbage,centerindex]=max(y);
	Pol = +1;
	disp('Pulse Polarity = Positive')

else
	[garbage,centerindex]=min(y);
	Pol = -1;
	disp('Pulse Polarity = Negative')
end

i = 2;
while sign(y(i)-lev50) == sign(y(i-1)-lev50)
	i = i+1;
end	%first crossing is between v(i-1) & v(i)

interp = (lev50-y(i-1)) / (y(i)-y(i-1));
tlead = x(i-1) + interp*(x(i)-x(i-1));
i = centerindex+1;
while ((sign(y(i)-lev50) == sign(y(i-1)-lev50)) & (i <= N-1))
	i = i+1;
end

if i ~= N
	Ptype = 1;
	disp('Pulse is Impulse or Rectangular with 2 edges')
	interp = (lev50-y(i-1)) / (y(i)-y(i-1));
	ttrail = x(i-1) + interp*(x(i)-x(i-1));
	width = ttrail - tlead;

else
	Ptype = 2;
	disp('Step-Like Pulse, no second edge')
	ttrail = NaN;
	width = NaN;

end
```

VITA

Hyungduk Ko is originally from Korea. In 2001, he received his B.S. in materials science and engineering and in 2003 he received his M.S. in materials science and engi-, neering both at Korea University. He received his Ph.D. in electrical engineering from Texas A&M University in 2009. His advisors were Dr. C. B. Su and Dr. M. Cheng. His research interests include nanophotonics and optics, plasmonic photonics, plasmonic-assisted optoelectronic device, solar cells and imaging and surface plasmon resonance (SPR) fiber optical sensors. He can be reached at the following address:

214 Zachry Engineering Center, Department of Electrical and Computer Engineering, Texas A&M University, College Station, TX 77843-3128